

Submitted to the Astrophysical Journal

The Spatial Distribution of Satellite Galaxies Selected from Redshift Space

Ingólfur Ágústsson & Tereasa G. Brainerd

Boston University, Institute for Astrophysical Research, 725 Commonwealth Ave., Boston, MA 02215

ingolfur@bu.edu, brainerd@bu.edu

ABSTRACT

We investigate the spatial distribution of satellite galaxies that were obtained from a mock redshift survey of the first Millennium Run simulation. The satellites were identified using typical redshift space criteria and, hence, the sample includes both genuine satellites and a large number of interlopers. As expected from previous work, the 3D locations of the satellites are well-fitted by a combination of a Navarro, Frenk & White (NFW) density profile and a power law. At fixed stellar mass, the NFW scale parameter, r_s , for the satellite distribution of red hosts exceeds that for the satellite distribution of blue hosts. In both cases the dependence of r_s on host stellar mass is well-fitted by a power law. For the satellites of red hosts, $r_s^{\text{red}} \propto (M_*/M_\odot)^{0.71 \pm 0.05}$ while for the satellites of blue hosts, $r_s^{\text{blue}} \propto (M_*/M_\odot)^{0.48 \pm 0.07}$. For hosts with stellar masses $M_* \gtrsim 4 \times 10^{10} M_\odot$, the satellite distribution around blue hosts is much more concentrated than is the satellite distribution around red hosts with the same stellar mass. We perform model fits to the projected (2D) locations of the satellites and find that, with the exception of the satellites of the most massive red hosts, the 2D analysis accurately recovers the values of r_s obtained from the 3D analysis. Therefore, even in the limit of a large number of interlopers, the 3D satellite distribution can be recovered using 2D information alone. The spatial distribution of the satellites of red hosts traces that of the hosts' halos; however, the spatial distribution of the satellites of blue hosts is more concentrated than that of the hosts' halos by a factor of ~ 2 . This calls into question whether observed satellites that are selected from redshift space can be used to directly infer the concentration of the dark matter halos of massive, blue host galaxies in our universe.

Subject headings: dark matter – galaxies: dwarf – galaxies: halos

1. Introduction

The spatial distributions of small, faint satellite galaxies have the potential to place strong constraints on the nature of the dark matter halos that surround the large, bright “host” galaxies about which the satellites orbit. Since the line of sight distances to the vast majority of galaxies are unknown, studies of satellite galaxies in our universe must rely upon methods other than physical distance to identify the objects of interest. Traditionally, satellite galaxies have been identified using proximity criteria that are implemented in redshift space, which necessarily requires both photometry and spectroscopy.

Using redshift space selection criteria, studies of the locations of the satellites of relatively isolated host galaxies have shown that, when the satellite locations are averaged over all satellites in the sample, the satellites are found preferentially close to the major axes of their hosts (e.g., Sales & Lambas 2004, 2009; Brainerd 2005; Azzaro et al. 2007; Ágústsson & Brainerd 2010, hereafter AB10; Ágústsson & Brainerd 2011). The projected locations of these satellites have also been shown to depend upon various physical properties of the hosts themselves (e.g. Azzaro et al. 2007; Siverd et al. 2009; AB10). The locations of the satellites of the host galaxies with the reddest colors and largest stellar masses are highly-anisotropic, and the satellites are located preferentially close to the major axes of their hosts. However, the locations of the satellites of the host galaxies with the bluest colors and the lowest stellar masses show little to no anisotropy (AB10). The host galaxies in these studies typically have stellar masses in the range $10^{10} M_{\text{sun}}$ to $10^{12} M_{\text{sun}}$ and, hence, their morphologies are likely to be “regular” (e.g., elliptical, spiral or lenticular). Therefore, the trend of observed satellite locations with the physical properties of the hosts is effectively a trend with host galaxy morphology since the reddest hosts are predominately ellipticals while the bluest hosts are predominately spirals.

Using simple assumptions about the ways in which luminous host galaxies might be embedded within their dark matter halos, Ágústsson & Brainerd (2006b) and AB10 showed that the observed locations of redshift space selected satellites can be easily reproduced from simulations of Λ -dominated Cold Dark Matter (CDM) universes. AB10 showed that the observed trends of projected satellite locations with host color and host stellar mass can only be reproduced if elliptical and non-elliptical (i.e., “disk”) hosts are embedded within their halos in different ways. Specifically, AB10 found that mass and light must be well-aligned in elliptical hosts, resulting from a model in which ellipticals are essentially miniature versions of their dark matter halos. In the case of the disk hosts, AB10 found that mass and light are poorly aligned, resulting from a model in which the angular momentum of the host’s disk is aligned with the angular momentum of its dark matter halo. Since the halo angular momentum vectors are not aligned with any of the halo principle axes (e.g., Bett et

al. 2007), misalignment of mass and light in disk hosts therefore occurs.

In addition to the locations of satellite galaxies relative to the mass and light of their host galaxies, redshift space selection of satellites has led to important conclusions about the nature of the dark matter halos surrounding field galaxies, based upon the kinematics of the satellites (e.g., McKay et al. 2002; Brainerd & Specian 2003; Prada et al. 2003; Conroy et al. 2005, 2007; Norberg et al. 2008; Klypin & Prada 2009; More et al. 2009, 2011), as well as the degree of intrinsic alignment of satellite galaxies with their hosts (Ágústsson & Brainerd 2006a). More recently, studies of satellite galaxies have been conducted using photometry alone (i.e., spectroscopy of the satellites is not necessary for these methods). Methods that rely on photometry alone have been shown to be a powerful way in which the satellite luminosity function, the projected satellite number density profile, and the small-scale clustering of satellite galaxies can be measured to the faintest possible limiting magnitudes (e.g., Guo et al. 2011; Lares et al. 2011; Nierenberg et al. 2011, 2012; Wang et al. 2011; Budzynski et al. 2012; Tal et al. 2012; Wang & White 2012; Wang et al. 2014).

The advantage to studies of satellite galaxies that do not rely on spectroscopy is that one can probe significantly fainter in the satellite population than one can probe with the current samples of satellites that have been selected from redshift space. This is accomplished by subtracting an average background galaxy number density from the vicinity of the host galaxies and results in a much larger sample of satellites on average than can be obtained using redshift space criteria. The disadvantage of photometric satellite studies, however, is that they cannot say with certainty whether any one particular faint galaxy is a satellite or whether it is, instead, a distant, unrelated background galaxy (i.e., since the method relies on the subtraction of an average background, not the identification of specific objects as satellites). The advantages of studies in which the satellites are selected from redshift space are: [1] the method identifies a specific set of faint galaxies as “the” satellites of the host galaxies and [2] these specific satellites can be linked directly to the masses of the hosts’ dark matter halos via their kinematics. Both of these methods (photometric and redshift space selection) are useful for studying the properties of satellite galaxies and both have the potential to place strong constraints on the nature of the dark matter distribution that surrounds the host galaxies.

Here we choose to focus on the spatial distribution of satellite galaxies that have been selected using redshift space criteria. We use a mock redshift survey of the first Millennium Run simulation¹ (MRS; Springel et al. 2005) to investigate the real space distribution of satellite galaxies around relatively isolated host galaxies, where the satellites are selected in

¹<http://www.mpa-garching.mpg.de/millennium>

the same way that one would select satellites from a redshift survey of our universe. The MRS followed the growth of structure in a Λ CDM cosmology ($H_0 = 73 \text{ km sec}^{-1} \text{ Mpc}^{-1}$, $\Omega_{m0} + \Omega_{b0} = 0.25$, $\Omega_{b0} = 0.04$, $\Omega_{\Lambda0} = 0.75$, $n = 1$, $\sigma_8 = 0.9$) from a redshift $z = 127$ to $z = 0$ using $N = 2160^3$ dark matter particles of mass $m_p = 8.6 \times 10^8 h^{-1} M_\odot$. The simulation volume is a cubical box with periodic boundary conditions and a comoving sidelength of $L = 500h^{-1} \text{ Mpc}$. A TreePM method was used to evaluate the gravitational force law, and a softening length of $5h^{-1} \text{ kpc}$ was used.

Previous studies of the spatial distributions of satellite galaxies in Λ CDM universes have focused on the distribution that results when the satellites are selected using full 3D information (i.e., not redshift space selection). Studies of the locations of luminous satellite galaxies obtained from semi-analytic galaxy formation models generally agree that, when selected in 3D, the satellites trace the dark matter distribution reasonably well, both within galaxy clusters and within individual, large host galaxies (e.g., Gao et al. 2004; Kang et al. 2005; Sales et al. 2007). Using gas dynamics simulations, however, Nagai & Kravtsov (2005) found that the concentration of the radial distribution of simulated cluster galaxies was systematically lower than that of the surrounding cluster dark matter.

Our work differs substantially from that of Sales et al. (2007), who also investigated the spatial distribution of satellite galaxies in the MRS. We select our host and satellite systems from redshift space in the same way as would be done for an observational sample, while Sales et al. (2007) selected hosts and satellites using the full 3D information that is available in the simulation. Of course, full 3D information is not generally available for an observational sample of host galaxies and their satellites (i.e., since the distances to the galaxies are usually not known). Here our sample of hosts and satellites is completely analogous to an observational sample, including the unavoidable presence of a significant number of false satellites (or “interlopers”) in the data (see §2). Here we aim to address three questions: [1] How does the spatial distribution of the satellite galaxies depend upon the color and stellar mass of the host galaxy? [2] Can the parameters associated with the spatial distribution of the satellite galaxies obtained with full 3D information be accurately recovered when only projected (i.e., 2D information) is used? and [3] To what degree does the satellite distribution trace the distribution of the dark matter surrounding the halos of the host galaxies?

The outline of the paper is as follows. In §2, we present the method we use to select relatively isolated host galaxies and their satellites, we describe the properties of the host-satellite samples that we use in our analysis, and we discuss the way in which we create “composite” host-satellite systems by stacking the data. In §3 we compute the 3D and 2D spatial distributions of the satellites and we determine the best-fitting model parameters

for the satellite distribution. In addition, in §3 we compare the spatial distribution of the satellites to the spatial distribution of the dark matter surrounding the host galaxies. In §4 we present a summary and discussion of our results.

2. Host–Satellite Sample

We are interested in the spatial distributions of satellite galaxies that have been selected via their proximity in redshift space, rather than their proximity real (i.e., 3D) space. That is, the satellites in which we are interested are small, faint objects that are located “close to” bright objects, both in projected radial distance on the sky, R_p , and in relative line of sight velocity, $|dv|$. Here we use the redshift space selection criteria from AB10, which yield a population of relatively isolated host galaxies and their satellites. The individual host galaxies dominate the kinematics of the systems and, for comparison, if the Local Group were viewed by an external observer, the Milky Way and M31 would likely be rejected as host galaxies because of their similar luminosities and their proximity to one another. Our selection criteria require that host galaxies be at least 2.5 times more luminous than any other galaxy that is found within a projected radial distance $R_p \leq 700$ kpc and a relative line of sight velocity $|dv| \leq 1000$ km sec^{−1}. Satellites must be found within a projected radial distance $R_p \leq 500$ kpc of their host and must have a relative line of sight velocity $|dv| \leq 500$ km sec^{−1}. In addition, each satellite must be at least 6.25 times fainter than its host. In order to eliminate a small number of systems that pass the above tests but which are likely to be clusters or groups (i.e., instead of relatively isolated host-satellite systems), we impose two further restrictions: [1] the luminosity of each host must exceed the sum total of the luminosities of its satellites, and [2] each host must have fewer than nine satellites. The choice of the maximum number of satellites is somewhat arbitrary and there is no significant effect on our results if we instead choose a different maximum value of, say, four or five satellites. This is due to the fact that most of our host galaxies have only one or two satellites (see Figure 1 of AB10), and the inclusion of a handful of systems with many satellites in the analysis does not affect our results in any significant way.

Our host-satellite sample is taken directly from AB10, and we refer the reader to AB10 for additional discussion of the sample. The hosts and satellites were obtained by implementing the above selection criteria for an all-sky mock redshift survey (Blaizot et al. 2005) of the first Millennium Run simulation (MRS; Springel et al. 2005), resulting in a total of 70,882 hosts and 140,712 satellites. From their B -band bulge-to-disk ratios, $\sim 30\%$ of the host galaxies are classified as ellipticals, while the rest are classified as disk galaxies (either spiral or lenticular). See AB10 and De Lucia et al. (2006) for details of the classification

scheme. In addition, we divide our host galaxy sample according to rest-frame optical color, $(g - r)$, at redshift $z = 0$. To do this, we fit the distributions of the host $(g - r)$ colors by the sum of two Gaussians (e.g., Strateva et al. 2001; Weinmann et al. 2006). The division between the two Gaussians lies at $(g - r) = 0.75$ and, therefore, we define “red” hosts to be those with $(g - r) \geq 0.75$ and “blue” hosts to be those with $(g - r) < 0.75$. See also AB10.

The mock redshift survey of the MRS was designed to reproduce the observed properties of the Sloan Digital Sky Survey (SDSS; e.g., Fukugita et al. 1996; Hogg et al. 2001; Smith et al. 2002; Strauss et al. 2002; York et al. 2000) and, hence, it has a relatively bright limiting magnitude. Because of this, only one or two satellites are typically identified for each host galaxy. Therefore, we investigate the spatial distribution of the satellite galaxies using ensemble averages. To do this, we stack many host-satellite pairs together, creating “composite” hosts, each of which have a large number of satellites after stacking. In order for this type of stacking to be reasonable, one has to be fairly certain that the vast majority of the hosts lie at the centers of their halos. While this may not be true for galaxies that dominate group systems (see, e.g., Skibba et al. 2011 and references therein), we know from AB10 that 94% of the host galaxies in our sample reside at the centers of their halos. Therefore, stacking of the individual host galaxies to create composite hosts is justified.

When creating the composite hosts, one would ideally stack together hosts whose dark matter halos have similar masses. While this could be done easily in the case of a simulation, halo mass is not something that is generally known for the host galaxies in an observational sample. In practice, therefore, it is not possible to use halo mass to stack together host galaxies in an observational sample. To make the best connection of theory to future observations, we choose to stack our simulated host galaxies using a method that could be implemented straightforwardly in a complimentary observational study. Since the luminosities and stellar masses of simulated galaxies are positively correlated with the masses of their dark matter halos (e.g., More et al. 2011 and references therein), it is possible to use either host luminosity or host stellar mass as a proxy for halo mass. Shown in the left panel of Figure 1 is the relationship between halo virial mass (M_{200}) and r -band absolute magnitude (M_r) for our host galaxies. Different point types and colors in Figure 1 indicate different morphologies for the host galaxies, as determined from their B -band bulge-to-disk ratios (see AB10). Orange contours indicate regions inside which $\sim 95\%$ of the red hosts are found and purple contours indicate regions inside which $\sim 95\%$ of the blue hosts are found. From the left panel of Figure 1, the spread in the relationship between halo virial mass and host luminosity is > 0.3 dex. Thus, a host galaxy with a given luminosity and morphology could have a dark matter halo mass that differs by more than a factor of two from that of another host with the identical luminosity and morphology. Also shown in Figure 1 (right panel) is the relationship between halo virial mass and stellar mass for our host galaxies. The

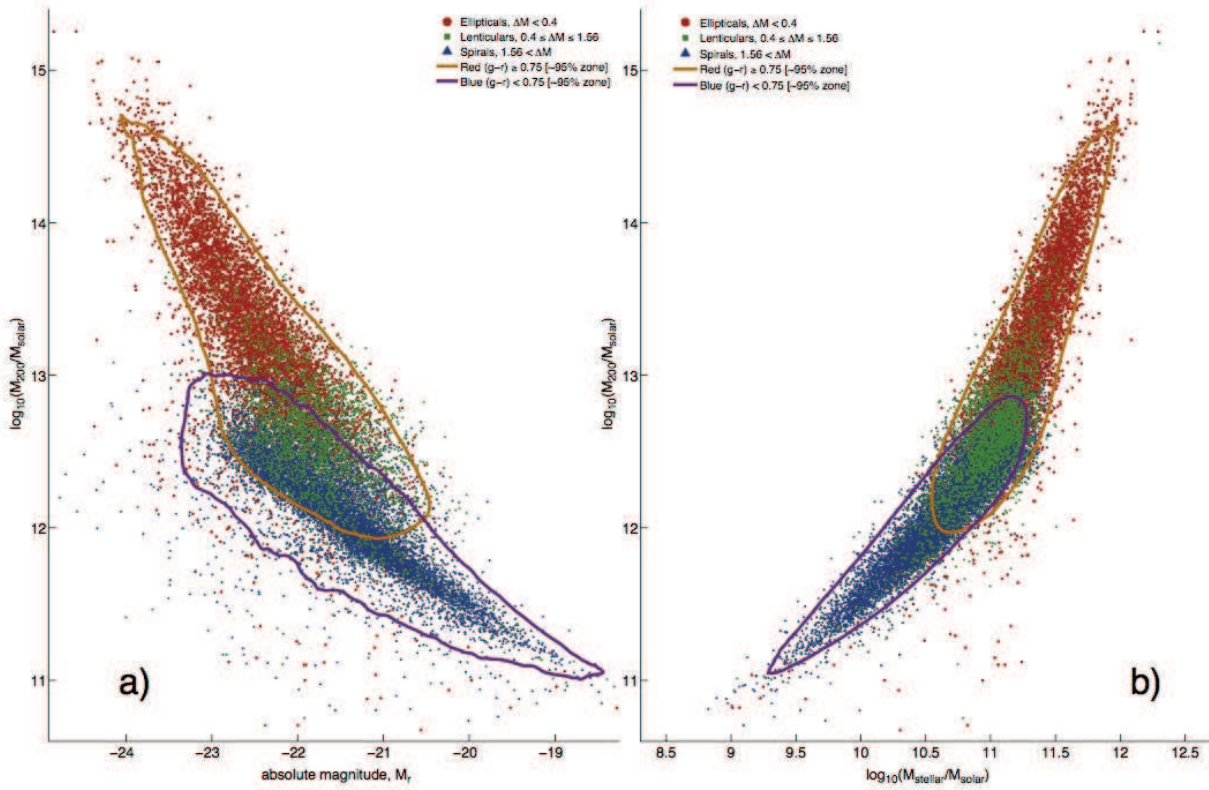


Fig. 1.— *Left:* Relationship between halo virial mass and r -band absolute magnitude for the host galaxies. *Right:* Relationship between halo virial mass and stellar mass for the host galaxies. In both panels different point types and colors indicate different host galaxy morphologies (red circles: elliptical; green squares: lenticular; blue triangles: spiral). Contours indicate regions inside which $\sim 95\%$ of the hosts of a given color are found.

relationship between halo virial mass and stellar mass is much tighter than the relationship between halo virial mass and host luminosity (i.e., the spread is $\lesssim 0.3$ dex). Therefore, it is preferable to use the hosts’ stellar masses, rather than their luminosities, when stacking the hosts together. The same conclusion was reached by Sales et al. (2007) in their study of MRS satellite galaxies that were selected using 3D spatial criteria.

Since there is a clear bimodal distribution of host galaxy colors, we construct our composite hosts by stacking together hosts of a given color (red or blue) within a given stellar mass range. Figure 2 shows the probability distributions for the stellar masses of the host galaxies, from which it is clear that the hosts with the lowest stellar masses are predominately blue, while the hosts with the highest stellar masses are predominately red. For our purposes we are primarily interested in being able to compare results for host galaxies with similar stellar masses, but different colors (i.e., red vs. blue). Therefore, we restrict our analysis to host galaxies with stellar masses in the range $10.3 \leq \log_{10} [M_*/M_\odot] \leq 11.5$, for which there are a significant number of both red and blue hosts with similar stellar masses (see Figure 2). To create the composite hosts, we adopt a fixed bin width of 0.3 dex in stellar mass (e.g., comparable to the error in the stellar mass estimates for SDSS galaxies; Conroy et al. 2009). Given the stellar mass range for the hosts, our analysis will concentrate on hosts that reside in one of four stellar mass bins: $10.3 \leq \log_{10} [M_*/M_\odot] < 10.6$ (bin B_1), $10.6 \leq \log_{10} [M_*/M_\odot] < 10.9$ (bin B_2), $10.9 \leq \log_{10} [M_*/M_\odot] < 11.2$ (bin B_3), and $11.2 \leq \log_{10} [M_*/M_\odot] \leq 11.5$ (bin B_4). When referring separately to the red or blue hosts within a given stellar mass bin we will use the notation B_1^{red} , B_1^{blue} , etc.

Tables 1 (red hosts) and 2 (blue hosts) show various statistics for the hosts and satellites as a function of host stellar mass. From left to right, the columns list the stellar mass bin, the number of hosts in the bin, the number of satellites in the bin, the number of satellites in the bin that are found within the halo virial radius (r_{200}), the median host stellar mass for the bin, the mean halo virial radius for the bin, and the mean halo virial mass (M_{200}) for the bin. Note that only 50% of all satellites in our sample are found within a 3D distance equal to the virial radii of their hosts (56% of the satellites of red hosts are found within a

Table 1. Red Host Statistics

Bin	N_{host}	N_{sat}	$N_{\text{sat}}(r_{200})$	Host $\log_{10} [M_{*,\text{med}}/M_\odot]$	Host $\langle r_{200} \rangle$ [kpc]	Host $\langle \log_{10} [M_{200}/M_\odot] \rangle$
B_1^{red}	817	1,348	504	10.53	226	12.2
B_2^{red}	5,003	9,561	4,202	10.80	285	12.5
B_3^{red}	12,244	26,073	13,156	11.07	368	12.8
B_4^{red}	10,863	27,220	18,101	11.33	550	13.3

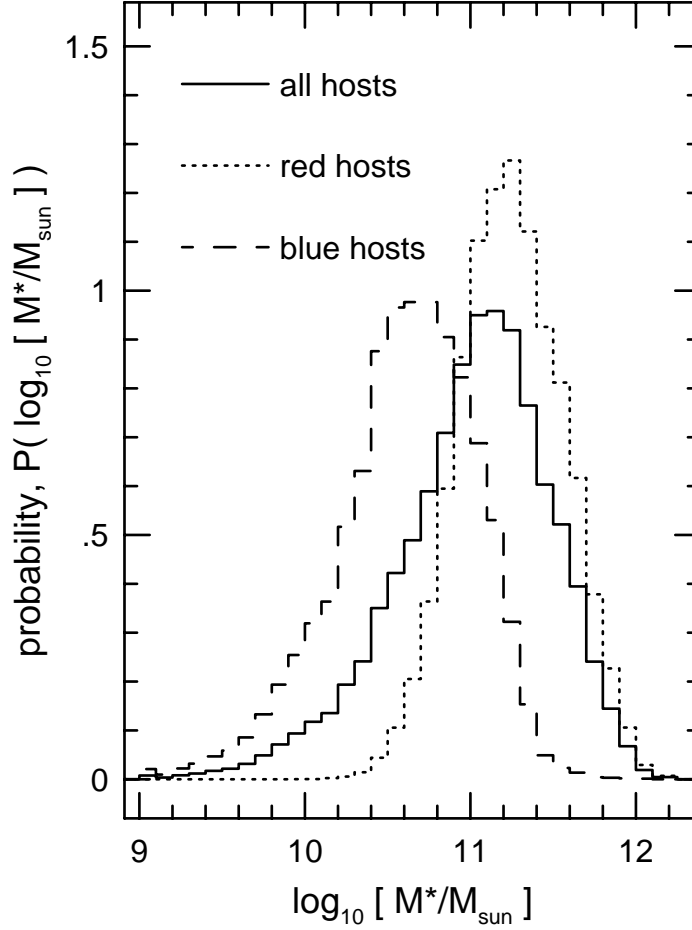


Fig. 2.— Probability distributions for the stellar masses of the host galaxies. Different line types indicate different types of hosts (solid lines: all hosts, dotted lines: red hosts, dashed lines: blue hosts). The majority of hosts with high stellar masses have rest-frame optical colors that are red, while the majority of hosts with low stellar masses have rest-frame optical colors that are blue.

Table 2. Blue Host Statistics

Bin	N_{host}	N_{sat}	$N_{\text{sat}}(r_{200})$	Host $\log_{10} [M_{*,\text{med}}/M_{\odot}]$	Host $\langle r_{200} \rangle$ [kpc]	Host $\langle \log_{10} [M_{200}/M_{\odot}] \rangle$
B_1^{blue}	7,984	11,831	3,636	10.47	195	12.0
B_2^{blue}	8,301	13,675	5,618	10.75	239	12.2
B_3^{blue}	5,287	9,765	4,329	11.03	294	12.5
B_4^{blue}	1,134	2,511	1,321	11.28	411	12.9

3D distance equal to r_{200} ; 39% of the satellites of blue hosts are found within a 3D distance equal to r_{200}). Further, 34% of all satellites in our sample are located more than 500 kpc from their host in 3D.

Throughout, it is important to keep in mind that, although the satellites we study here are a subset of the satellites that would be selected using 3D spatial locations, the subset is not random. A sample of satellites that is selected using redshift space criteria may therefore yield different conclusions than a sample of satellites that is selected using 3D spatial criteria. Samples of satellites that are selected using redshift space criteria are necessarily incomplete because of the nature of the selection criteria themselves. The incompleteness compared to 3D selection is due in part to the fact that current redshift surveys have relatively bright limiting magnitudes. That is, only the intrinsically brightest one or two satellites are selected for any given host galaxy, with the apparent magnitude difference between the hosts and satellites being typically in the range of $\Delta r \sim 2$ to $\Delta r \sim 2.5$ (see, e.g., Figure 1 of Ágústsson & Brainerd 2006a). In particular, when Sales et al. (2007) selected satellite galaxies in 3D from the MRS, they found 2.3 times more satellites within their hosts’ virial radii than we have in our sample. The larger, brighter satellites that result from redshift space selection may have distributions that differ from those of more “typical” satellites. In addition, satellites with velocities that are high relative to their hosts (but which are nevertheless bound to their hosts) will be rejected from samples that are selected in redshift space because the selection criteria impose a maximum value for the host-satellite relative velocity, $|dv|$. It is, of course, possible to increase the maximum host-satellite relative velocity in order to capture additional, genuine high velocity satellites. However, for the selection criteria that we adopt here, this would come at the expense of significantly increased “noise” in the form of a much larger interloper fraction in the host-satellite sample.

Despite the similar stellar masses of the red and blue hosts within a given bin, Tables 1 and 2 show that the halos of the red hosts are generally more massive than those of the blue hosts. Within all of the stellar mass bins, the ratio of the median host stellar masses is $M_{*,\text{med}}^{\text{red}}/M_{*,\text{med}}^{\text{blue}} \lesssim 1.15$, while the ratio of the median host halo virial masses is $M_{200,\text{med}}^{\text{red}}/M_{200,\text{med}}^{\text{blue}} \gtrsim 1.5$. In addition, it is clear from Tables 1 and 2 that each of the stellar mass bins contains hosts with a wide range of halo virial masses (i.e., the scatter between adjacent bins is ~ 0.3 dex), so there is necessarily some overlap between the halo masses within adjacent stellar mass bins.

Figure 3 shows the mean halo mass for the hosts as a function of stellar mass for the red hosts (top panel) and the blue hosts (bottom panel). Shown for comparison (solid line) is the relationship between mean halo mass and stellar mass for the entire population of galaxies in the two Millennium simulations from Guo et al. (2010), which itself agrees reasonably

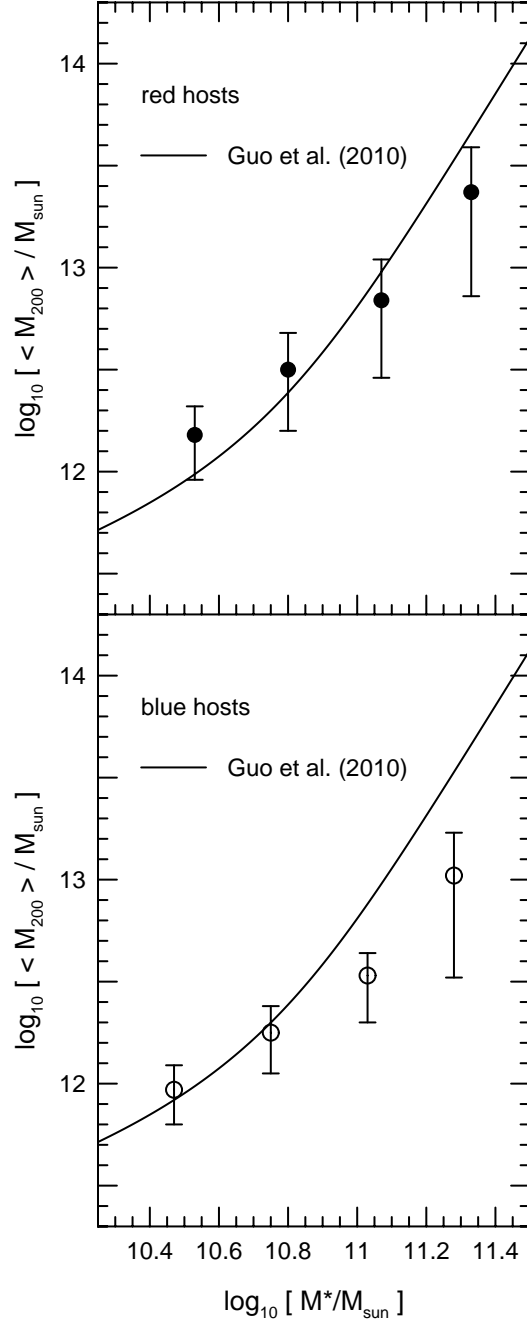


Fig. 3.— Relationship between stellar mass and halo virial mass for the host galaxies. Error bars indicate 68% confidence limits. Also shown (solid line) is the relationship between stellar mass and halo mass from Guo et al. (2010). *Top*: Red hosts. *Bottom*: Blue hosts.

well with observational estimates of the halo mass-stellar mass relationship for the galaxy population on average. In the case of our red hosts, all but the most massive hosts (bin B_4^{red}) lie on the relationship found by Guo et al. (2010). In the case of our blue hosts, it is only the least massive hosts (bins B_1^{blue} and B_2^{blue}) that lie on the relationship found by Guo et al. (2010). It is important to keep in mind that our host galaxies are not selected to be “average” galaxies; instead they are examples of large, bright galaxies that are relatively isolated within their local regions of space (i.e., we specifically reject galaxies as hosts if they reside in particularly high density regions of space). Figure 3 suggests that the host galaxies in the lower stellar mass bins have dark matter halos that are similar to those of average galaxies. This is reasonable because, on average, galaxies with low stellar masses tend to be less clustered than galaxies with high stellar masses (e.g., Li et al. 2006).

3. Satellite Spatial Distributions: 3D vs. 2D

Full knowledge of the 3D distribution of galaxies is one of the great luxuries of numerical simulations. In the observed universe, however, one is restricted to a coordinate system that consists only of the redshifts of the galaxies and their locations on the celestial sphere. In this section we begin by investigating the 3D spatial distribution of satellite galaxies that is obtained when the satellites have been selected using redshift space criteria (i.e., exactly as must be done when obtaining a sample of “spectroscopically selected” satellites from a large redshift survey such as the SDSS). Here we seek an analytic density profile that describes the 3D distribution of the satellites around their hosts. In addition, we wish to parameterize the density profile in such a way that the parameters can be obtained from the type of 2D satellite distribution that one would have in an observational redshift survey (i.e., in a redshift survey one can only quantify the satellite locations in terms of their projected radial distances from their hosts).

To begin, let us consider the real space volume within which the satellites are contained. Because of the nature of the redshift space selection criteria (i.e., satellites must be found within a given maximum projected radial distance of their hosts, as well as a given line of sight velocity relative to their hosts), the satellites are effectively found within a cylindrical volume, where the axis of the cylinder is the line of sight to the host. Technically, the geometry is closer to being a topeless cylindrical cone, since the selection criteria make use of angular separations on the sky, as well angular diameter distances that are calculated using the redshifts of the hosts. However, the difference from a cylindrical volume is small and here we simply adopt the cylindrical geometry (which, for practical purposes, is all that could be done in an observational survey where the actual distances to the galaxies are not

known). The cylindrical nature of the selection volume is clear from Figure 4, which shows a composite of the real space locations of the satellite galaxies from AB10. The locations of the satellites are plotted relative to the locations of their hosts. The redshift space selection criteria result in the maximum line of sight separation between the hosts and satellites in AB10 being ~ 10 Mpc; however, 74% of the satellites in AB10 are found within 500 kpc of their host along the line of sight, and 84% are found within 1 Mpc along the line of sight (see Figure 5, which shows the distribution of line of sight separations for the hosts and satellites in AB10). From Figures 4 and 5, then, the redshift space selection criteria result in a sample of satellites whose locations are sharply peaked at the locations of their hosts. Nevertheless it is also important to note that the tails of the distribution are long. This is due to the fact that the redshift space selection criteria cannot distinguish between relative line of sight velocities that are caused by the Hubble flow and those that are caused by the peculiar velocities of satellites moving within the gravitational potentials of their hosts’ halos.

Figures 4 and 5 also emphasize an important point regarding the nature of the interlopers. Although the interlopers in a spectroscopically-selected sample are often treated as a random population, this is not actually the case (see, e.g., McKay et al. 2002; Brainerd & Specian 2003; Prada et al. 2003; van den Bosch 2004; Ágústsson 2011). Instead, the vast majority of interlopers are members of the local large scale structure that surrounds the host galaxies and they are, therefore, intrinsically clustered with both the host galaxies and their genuine satellites.

For convenience, we take the origin of the cylindrical coordinate system in which the satellites are found to be the location of the composite host galaxy. We take the axis of the cylinder to be the line of sight, which in real space corresponds to a coordinate

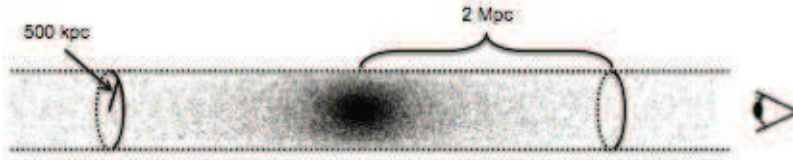


Fig. 4.— Composite of the real space locations of the satellite galaxies from AB10 illustrating the large-scale cylindrical nature of the selection criteria. Only satellites located within ± 3 Mpc along the line of sight to their hosts are shown in this figure. For 3D distances $r < 500$ kpc, the geometry of the satellite distribution is essentially spherical, while for $r \gg 500$ kpc the satellite distribution is cylindrical. This marked change in geometry causes a discontinuity in the number of satellites as a function of 3D distance at $r \sim R_{\text{max}} = 500$ kpc (see text).

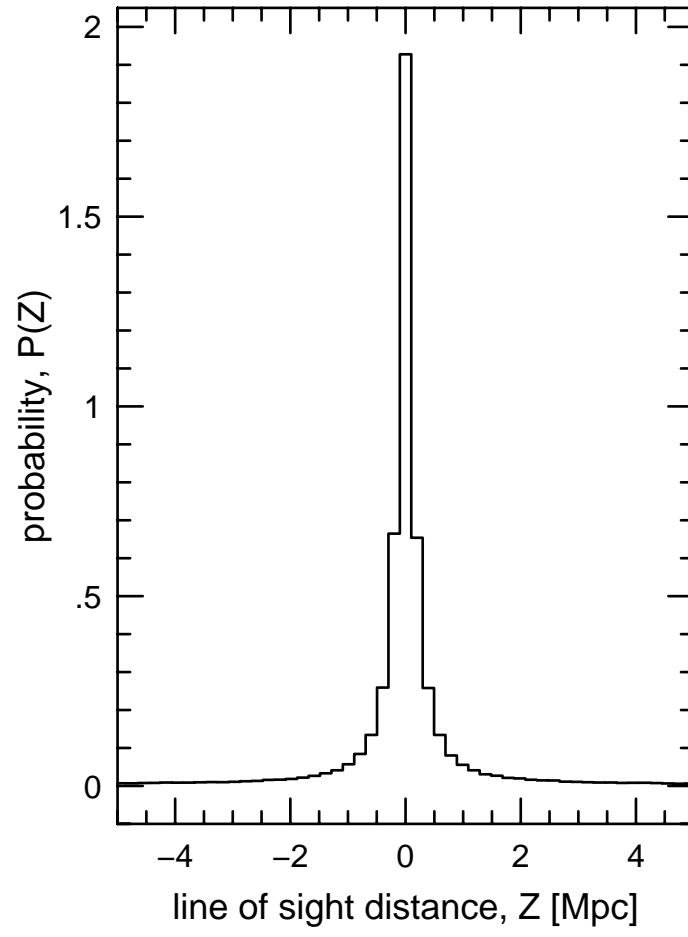


Fig. 5.— Probability distribution for the line of sight distances between the hosts and satellites from AB10.

we label as Z . The satellites do not extend to infinite distances along the line of sight. Instead, they are confined to a cylindrical volume that extends to coordinates $\pm Z_{\max}$, relative to the host. Further, we take the projected radial distance, R_p , between the hosts and satellites to be the radial coordinate for the cylindrical system. The selection criteria impose a maximum projected radial distance of $R_{\max} \equiv R_{p,\max} = 500$ kpc. For our calculations below we also impose a formal minimum projected radial distance for the hosts and satellites, $R_{\min} \equiv R_{p,\min} = 25$ kpc. The reason for including a minimum distance is that we expect to find few satellites in an observational sample with a projected radial distance $R_p \leq 25$ kpc due to the fact that such nearby satellites are generally difficult to distinguish from their hosts in the imaging data.

Figure 6 shows the probability distributions for the 3D distances between the hosts and their satellites. The probability distributions peak at small values of r and they exhibit long tails that extend far beyond the maximum values of r that are shown in Figure 6. Approximately 90% of the satellites are found within a 3D distance of $r \leq 1$ Mpc from their hosts. Approximately 6% of the satellites are found beyond a 3D distance of $r = 3.5$ Mpc from their hosts, and $\lesssim 1\%$ are found as far as 10 Mpc from their hosts. The existence of such long tails in the distributions of the 3D satellite distances gives rise to a relatively flat distribution of 2D satellite locations at large projected radii (i.e., due to the fact that, in projection, the distributions have been integrated along the line of sight). The probability distributions for the 2D satellite locations are shown in Figure 7. In almost all cases, the distribution of the 3D distances between the hosts and satellites changes markedly at $r \sim R_{\max} = 500$ kpc (i.e., there is a clear discontinuity in the functions at 500 kpc). This marked change is due to a manifestation of the overall cylindrical nature of the selection criteria. For 3D distances $r \leq R_{\max}$, the selection criteria collect essentially all satellites within a sphere of radius R_{\max} . For 3D distances $r > R_{\max}$, the selection criteria select only satellites that are found within a projected radial distance $R_p \leq R_{\max}$. It is, therefore, at 3D distances of $r \sim R_{\max}$ that the distribution of satellite locations changes from being spherical to being cylindrical. Below we will explicitly account for this change in geometry when we model the number density of satellites as a function of their distances from the hosts.

3.1. 3D Satellite Number Density

We denote the 3D number density profile of the satellites by $\nu(r)$. The differential satellite number count is then simply the number of satellites that are found within the infinitesimal interval $[r, r + dr]$,

$$dN(r) = \int_S \nu(r) dS dr . \quad (1)$$

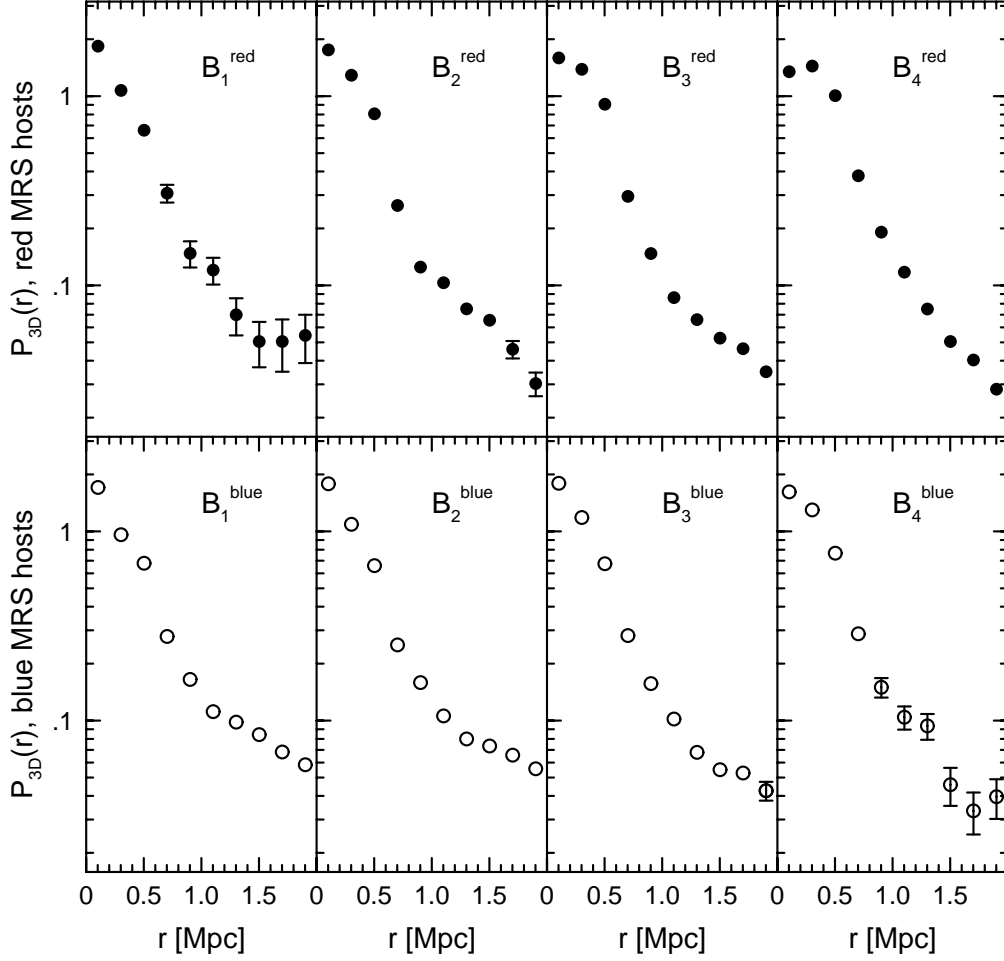


Fig. 6.— Probability distributions for the 3D distances between the hosts and satellites. Error bars are omitted when they are comparable to or smaller than the sizes of the data points. Note that in most cases a discontinuity occurs at $r \sim 500$ kpc, corresponding to the change in geometry from spherical to cylindrical for the satellite locations. *Top*: Red hosts. *Bottom*: Blue hosts.

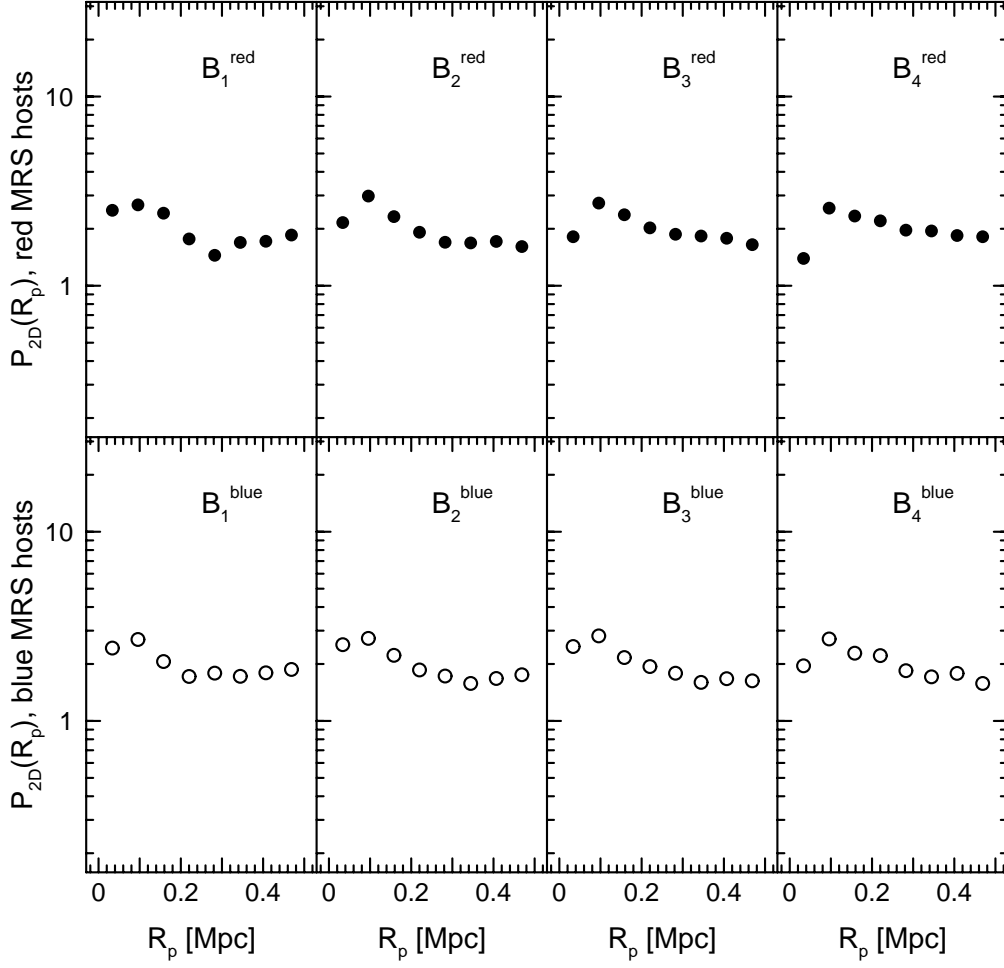


Fig. 7.— Probability distributions for the projected (2D) distances between the hosts and satellites. Error bars are omitted since they are comparable to or smaller than the sizes of the data points. *Top*: Red hosts. *Bottom*: Blue hosts.

Here S is the area of the spherical surface at radius r that is contained within a cylinder of radius R_{\max} . When $r \leq R_{\max}$, the surface S covers the entire sphere (i.e., an area of $4\pi r^2$). For $r > R_{\max}$ the surface S covers two spherical caps, where each cap has a base of radius R_{\max} and height $r - \sqrt{r^2 - R_{\max}^2}$. The surface area of a spherical cap is equal to the area of a circle whose radius equals the distance between the vertex and the base of the cap. Therefore, for $r > R_{\max}$ we have that the surface area, S , is given by $2\pi \left[R_{\max}^2 + \left(r - \sqrt{r^2 - R_{\max}^2} \right)^2 \right] = 4\pi \left(r^2 - r \sqrt{r^2 - R_{\max}^2} \right)$, where the factor of two accounts for the presence of both spherical caps. We then have

$$dN(r) = \begin{cases} 4\pi r^2 \nu(r) dr, & r \leq R_{\max} \\ 4\pi \left(r^2 - r \sqrt{r^2 - R_{\max}^2} \right) \nu(r) dr, & r > R_{\max} \end{cases} \quad (2)$$

Equivalently, we can write the differential number count as a single mathematical expression,

$$dN(r) = 4\pi \left[r^2 - r \sqrt{\mathcal{R}(r^2 - R_{\max}^2)} \right] \nu(r) dr, \quad (3)$$

where $\mathcal{R}(x)$ is the ramp function: $\mathcal{R}(x) = x$ for $x \geq 0$ and $\mathcal{R}(x) = 0$ otherwise. Finally, the interior number count is simply the cumulative number of satellites that are enclosed within a 3D distance r ,

$$N(< r) = \int_0^r dN(r) \quad (4)$$

Although our satellite sample is not a random subset of the satellites that would be selected if 3D spatial criteria were used, we can nevertheless anticipate the functional form that $\nu(r)$ will take based upon previous work. First, we know that the selection criteria yield a sample of objects that consists both genuine satellites and interlopers (see, e.g., AB10 and references therein). Sales et al. (2007) studied the locations of the satellites of isolated galaxies in the MRS, where the satellites were selected using their 3D locations relative to the host galaxies, not redshift space criteria. From their work, Sales et al. (2007) found that the number density of the 3D selected satellites was well-fitted by a Navarro, Frenk and White profile (NFW; Navarro, Frenk & White 1995, 1996, 1997) for host-satellite distances $r \lesssim 2 r_{200}$. Similarly, Kang et al. (2005) found that when satellites of Milky Way-type halos were selected in 3D, the satellites traced the dark matter distribution well, particularly for radii between $0.1 r_{\text{vir}}$ and r_{vir} . Thus, in our host-satellite sample we expect that for small values of the 3D host-satellite distance, $\nu(r) \propto (r/r_s)^{-1} (1 + r/r_s)^{-2}$, where r_s is the NFW scale radius. For large values of r the hosts and satellites in our sample should not be kinematically related (i.e., for large values of r the “satellites” are actually interlopers). Therefore, on large scales the form of the probability density for the separation between hosts and satellites should be the same as the probability density for the separation between

galaxies as a whole, which is approximated well by a power law (e.g., Hayashi & White 2008). For large values of r , then, we would expect $\nu(r) \propto r^{-\gamma}$.

For simplicity we adopt a functional form for the satellite number density that consists of a superposition of an untruncated NFW profile and a power law:

$$\nu(r) \equiv \frac{A}{r/r_s (1 + r/r_s)^2} + \frac{C}{r^\gamma}, \quad (5)$$

where A and C are constants. So long as $\gamma < 3$, the interior number count will be finite. The above model for the satellite number density describes the combination of two populations of objects that are fundamentally impossible to distinguish in a sample of satellites that has been selected using redshift space criteria: one population (the genuine satellites) has a number density that behaves like an NFW profile, the other population (the interlopers) has a number density that falls off as some power of the distance. On large scales, the NFW profile falls off as r^{-3} , so that again as long as $\gamma < 3$, the number density of satellites at large distances from the host galaxy becomes dominated by the interlopers that reside within the tails of the distribution. Throughout the discussion below we will refer to these distant objects as “tail interlopers”. When applied to the dark matter halos of galaxies, the NFW profile is technically only valid within the virial radii of the halos. For convenience, however, we extend the NFW profile beyond the virial radii of the hosts in order to smoothly capture the behavior of $\nu(r)$ at radii that are in between those at which the pure NFW profile and the pure power law separately dominate.

Below we treat the NFW component of the satellite number counts separately from that of the tail interlopers. To do this, we make the definitions $\nu(r)_{\text{NFW}} \equiv A(r/r_s)^{-1}(1 + r/r_s)^{-2}$ and $\nu(r)_{\text{tail}} \equiv Cr^{-\gamma}$. Using Equations (3) and (4), the 3D differential and interior number counts of the satellites in the NFW component are then given by

$$dN_{\text{NFW}}(r) = 4\pi A r_s \frac{r - \sqrt{\mathcal{R}(r^2 - R_{\text{max}}^2)}}{(1 + r/r_s)^2} dr \quad (6)$$

$$N_{\text{NFW}}(< r) = 4\pi A r_s^3 \left[\ln(1 + r/r_s) - \frac{r/r_s}{1 + r/r_s} - g_{\text{NFW}}(r) \right], \quad (7)$$

where

$$g_{\text{NFW}}(r) = \begin{cases} 0 & r \leq R_{\text{max}} \\ \cosh^{-1}\left(\frac{r}{R_{\text{max}}}\right) - \frac{\sqrt{r^2 - R_{\text{max}}^2}}{r + r_s} - \frac{r_s \cos^{-1}\left(\frac{rr_s + R_{\text{max}}^2}{(r + r_s)R_{\text{max}}}\right)}{\sqrt{R_{\text{max}}^2 - r_s^2}} & r > R_{\text{max}} \end{cases} \quad (8)$$

The 3D differential and interior number counts of the tail interlopers are given by

$$dN_{\text{tail}} = 4\pi C r^{-\gamma} \left[r^2 - r\sqrt{\mathcal{R}(r^2 - R_{\text{max}}^2)} \right] dr \quad (9)$$

$$N_{\text{tail}}(< r) = 4\pi C \left[(3 - \gamma)^{-1} r^{(3-\gamma)} - R_{\text{max}}^{(3-\gamma)} g_{\text{tail}}(r/R_{\text{max}}) \right] , \quad (10)$$

where

$$g_{\text{tail}}(x) = \begin{cases} 0 & x \leq 1 \\ \frac{1}{2} [x\sqrt{x^2 - 1} - \cosh^{-1}(x)] & x > 1, \gamma = 1 \\ \frac{1}{(3-\gamma)(\gamma-1)} \left[\frac{\sqrt{x^2-1}}{x^\gamma} \{(\gamma-1)x^2 + 1\} + \frac{\gamma}{2} B\left(x^{-2}; \frac{\gamma+1}{2}, \frac{1}{2}\right) - \frac{\sqrt{\pi}\Gamma(\frac{\gamma+1}{2})}{\Gamma(\frac{\gamma}{2})} \right] & x > 1, \gamma \neq 1 \end{cases} . \quad (11)$$

Here $B(y; a, b) \equiv \int_0^y t^{a-1} (1-t)^{b-1} dt$ is the incomplete Beta function.

3.2. 2D Satellite Number Density

The surface number density of the satellites as a function of projected radial distance, R_p , is obtained by integrating the 3D number density along the line of sight, $\Sigma(R_p) = \int \nu(\sqrt{R_p^2 + Z^2}) dZ$. The satellites are confined to a cylinder of length $2Z_{\text{max}}$ (i.e., the line of sight coordinates of the satellites are confined to $|Z| \leq Z_{\text{max}}$, centered on the hosts), and therefore the surface number density becomes

$$\Sigma(R_p) = 2 \int_{R_p}^{\sqrt{R_p^2 + Z_{\text{max}}^2}} \frac{\nu(r) r}{\sqrt{r^2 - R_p^2}} dr , \quad (12)$$

where r is the 3D distance.

As in the previous section, we treat the satellites in the NFW component separately from the tail interlopers. Using $\nu_{\text{NFW}}(r)$ in Equation (12) above, we find that the surface number density of the satellites in the NFW component is given by

$$\Sigma_{\text{NFW}}(R_p) = \frac{2Ar_s}{(R_p/r_s)^2 - 1} \left[\frac{Z_{\text{max}}/r_s}{1 + \sqrt{(R_p/r_s)^2 + (Z_{\text{max}}/r_s)^2}} - \frac{\sin^{-1} \left(\frac{Z_{\text{max}}}{R_p} \frac{\sqrt{(R_p/r_s)^2 - 1}}{1 + \sqrt{(R_p/r_s)^2 + (Z_{\text{max}}/r_s)^2}} \right)}{\sqrt{(R_p/r_s)^2 - 1}} \right] \quad (13)$$

(c.f. Bartelmann 1996). The differential number count for the satellites in the NFW component, as seen in projection on the sky, is then $dN_{p,\text{NFW}}(R_p) = 2\pi R_p \Sigma_{\text{NFW}}(R_p) dR_p$. Using Equation (13) above for Σ_{NFW} we find that the interior number count of satellites in the NFW component, as seen in projection on the sky, is

$$N_{p,\text{NFW}}(< R_p) = 4\pi A r_s^3 \left[\ln \left(1 + \frac{Z_{\text{max}}}{r_s} \right) - \sinh^{-1} \left(\frac{Z_{\text{max}}}{R_p} \right) + \frac{1}{\sqrt{(R_p/r_s)^2 - 1}} \sin^{-1} \left(\frac{Z_{\text{max}}}{R_p} \frac{\sqrt{(R_p/r_s)^2 - 1}}{1 + \sqrt{(R_p/r_s)^2 + (Z_{\text{max}}/r_s)^2}} \right) \right] . \quad (14)$$

Similarly, the differential number count for the tail interlopers, as seen in projection, is given by $dN_{p,\text{tail}}(R_p) = 2\pi R_p \Sigma_{\text{tail}}(R_p) dR_p$, where

$$\Sigma_{\text{tail}}(R_p) = \begin{cases} \frac{2C}{(\gamma-1)R_p^{(\gamma-1)}} \left[\frac{\sqrt{\pi}\Gamma(\frac{\gamma+1}{2})}{\Gamma(\frac{\gamma}{2})} - \frac{Z_{\text{max}} R_p^{(\gamma-1)}}{(R_p^2 + Z_{\text{max}}^2)^{\gamma/2}} - \frac{\gamma}{2} B\left(\frac{R_p^2}{R_p^2 + Z_{\text{max}}^2}; \frac{\gamma+1}{2}, \frac{1}{2}\right) \right] & \gamma \neq 1 \\ 2C \sinh^{-1}\left(\frac{Z_{\text{max}}}{R_p}\right) & \gamma = 1 \\ \frac{2C}{R_p} \cot^{-1}\left(\frac{R_p}{Z_{\text{max}}}\right) & \gamma = 2. \end{cases} \quad (15)$$

The interior number count of the tail interlopers, as seen in projection, is therefore

$$N_{p,\text{tail}}(< R_p) = \begin{cases} 2\pi C \frac{R_p^{(3-\gamma)}}{(3-\gamma)} \left[\frac{\sqrt{\pi}\Gamma(\frac{\gamma-1}{2})}{\Gamma(\frac{\gamma}{2})} - \frac{\gamma}{\gamma-1} B\left(\frac{R_p^2}{R_p^2 + Z_{\text{max}}^2}; \frac{\gamma+1}{2}, \frac{1}{2}\right) \right] + \\ 4\pi C \frac{Z_{\text{max}}}{(3-\gamma)(\gamma-2)} \left[Z_{\text{max}}^{(2-\gamma)} - \frac{(2\gamma-3)R_p^2 + (\gamma-1)Z_{\text{max}}^2}{(\gamma-1)(R_p^2 + Z_{\text{max}}^2)^{\gamma/2}} \right] & \gamma \neq 1, 2 \\ 2\pi C \left[R_p^2 \sinh^{-1}\left(R_p^{-1} Z_{\text{max}}\right) + Z_{\text{max}} \left(\sqrt{R_p^2 + Z_{\text{max}}^2} - Z_{\text{max}} \right) \right] & \gamma = 1 \\ 4\pi C \left[R_p \cot^{-1}\left(R_p Z_{\text{max}}^{-1}\right) + Z_{\text{max}} \ln\left(Z_{\text{max}}^{-1} \sqrt{R_p^2 + Z_{\text{max}}^2}\right) \right] & \gamma = 2. \end{cases} \quad (16)$$

3.3. 3D and 2D Model Parameters for the Spatial Distribution of Satellites

We next use a Maximum Likelihood (ML) method to obtain the best-fitting model parameters and corresponding errors for the satellite number density in each of our host galaxy stellar mass bins. We evaluate the goodness of fit using a combination of the Kolmogorov-Smirnov (KS) statistic and bootstrap resampling (e.g., Babu & Feigelson 2006). Bootstrap resampling is necessary since the default rejection confidence levels from the KS statistic, $(1 - P_{\text{KS}}) \times 100\%$, are not reliable when the parameters of the model are determined from the data (e.g., Lilliefors 1969). Here we use non-parametric bootstrap resampling, in which the bootstrap sample is drawn directly from the data. Each bootstrap sample then represents one possible realization of the hosts and satellites, and throughout we apply the ML fitting procedure separately to each of the different realizations. We compute the goodness of the model fits using the distribution of the deviations of the bootstrapped data from the model, which results in unbiased rejection confidence levels. Throughout, we obtain the bootstrap samples by repeatedly drawing (with replacements) from the host sample. It is important to resample the hosts since the satellites are not all independent of each other (i.e., some satellites belong to the same host). By resampling using the hosts, we insure that an individual bootstrap sample will contain all of the host-satellite pairs for a given host.

In order to implement the ML fitting procedure, we define a probability density function

for the 3D distribution of the satellite galaxies of the form

$$P_{3D}(r) \equiv (1 - f_{\text{tail}})P_{\text{NFW}}(r) + f_{\text{tail}}P_{\text{tail}}(r) , \quad (17)$$

where $0 \leq f_{\text{tail}} \leq 1$ is the fraction of tail interlopers in the sample. Here $P_{\text{NFW}}(r)$ and $P_{\text{tail}}(r)$ are probability density functions for the NFW component and the tail interlopers, respectively. The individual probability density functions, $P_{\text{NFW}}(r)$ and $P_{\text{tail}}(r)$, are based on the interpretation of the differential number counts of the satellites, dN , as the unnormalized probability of finding a satellite within the infinitesimal interval $[r, r + dr]$.

The probability density function has three free parameters from the model: r_s , γ , and f_{tail} . It also has three geometrical parameters, two of which are known from the selection criteria: R_{min} and R_{max} , the minimum and maximum projected distances. The third geometrical parameter, r_{max} , is the length of the tail of the satellite distribution in 3D which is, of course, not known for an observational sample of hosts and satellites. Figures 8, 9, and 10 show the model parameters r_s , γ , and f_{tail} from the 3D ML fits that were computed by adopting five different values of r_{max} (1, 2, 3.5, 5, and 7 Mpc), which enclose 83%, 90%, 94%, 96%, and 98% of all satellites, respectively. From Figure 8, it is clear that r_s increases with increasing host stellar mass, the best-fitting value of r_s is not particularly sensitive to the value of r_{max} that is adopted and, within a given stellar mass bin, the best-fitting value of r_s is larger for the satellites of red hosts than it is for the satellites of blue hosts.

Shown in Figure 9 are the best-fitting values of the power law index, γ . From this figure it is clear that, with the exception of the satellites of the B_4^{red} hosts, the best-fitting value of γ is only weakly-dependent on the value of r_{max} as long as $r_{\text{max}} \geq 3.5$ Mpc. In particular, for $r_{\text{max}} = 3.5$ Mpc, $\gamma \simeq 0.8$ for all of the satellites except those of the B_4^{red} hosts. Figure 10 shows that, again with the exception of the satellites of the B_4^{red} hosts, the value of f_{tail} increases monotonically with r_{max} , as expected (i.e., as r_{max} increases we are integrating out to larger and larger distances, where the tail interlopers dominate the sample). The different behavior of the fits for the satellites of the B_4^{red} hosts is almost certainly connected to our satellite selection criteria. That is, we select only those satellites whose velocities, relative to their hosts, are $|dv| \leq 500 \text{ km sec}^{-1}$. The B_4^{red} hosts have the most massive halos (mean virial mass of $\sim 2.3 \times 10^{13} M_{\odot}$) and, hence, the highest velocity dispersions ($\sigma_v \sim 320 \text{ km sec}^{-1}$). Therefore, it is likely that the sample of satellites around the B_4^{red} hosts is incomplete since our selection criteria only allow for maximum relative velocities that are $\sim 50\%$ greater than the expected velocity dispersion of the hosts' halos. In other words, in the case of the B_4^{red} hosts, it is likely that our satellite sample is not fully-representative of the satellite distribution around these particular hosts. From Figure 10, the tail interloper fraction for the satellites of the blue hosts always exceeds that for the satellites of the red hosts (again with the exception of the satellites around the B_4^{red} hosts). This is expected since there is

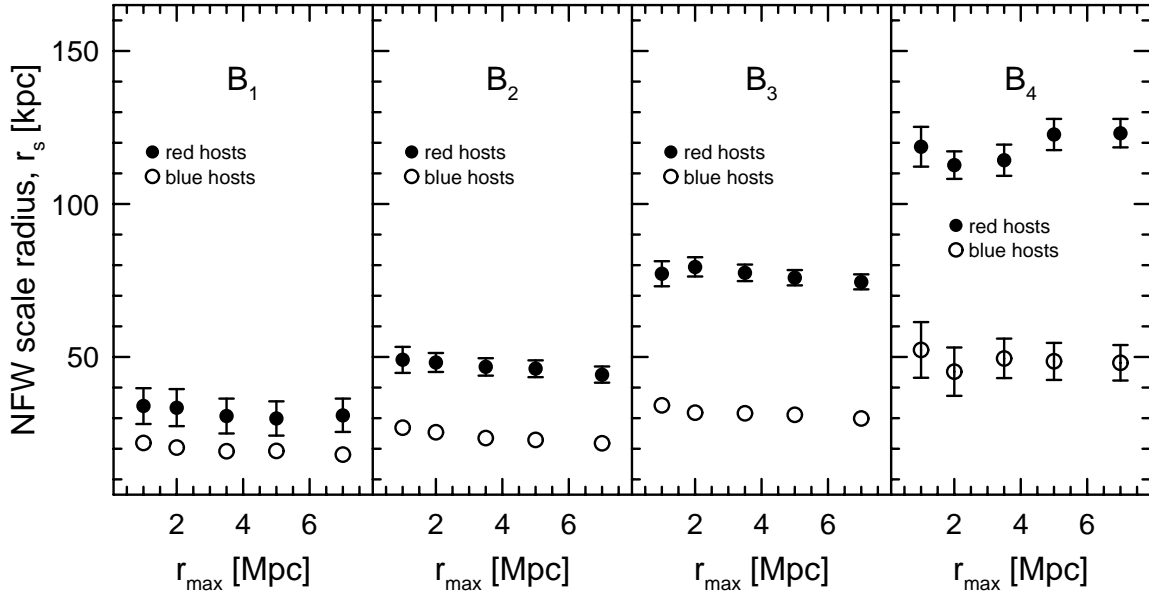


Fig. 8.— Best-fitting values of the NFW scale parameter, r_s , as a function of r_{\max} for satellites surrounding hosts of different stellar masses. Here a fit to the 3D satellite locations has been performed. Error bars are omitted when they are comparable to or smaller than the sizes of the data points. The best-fitting values of r_s are insensitive to the value of r_{\max} that is adopted. Within a given host stellar mass bin, the value of r_s for the satellites of the red hosts exceeds that for the satellites of the blue hosts.

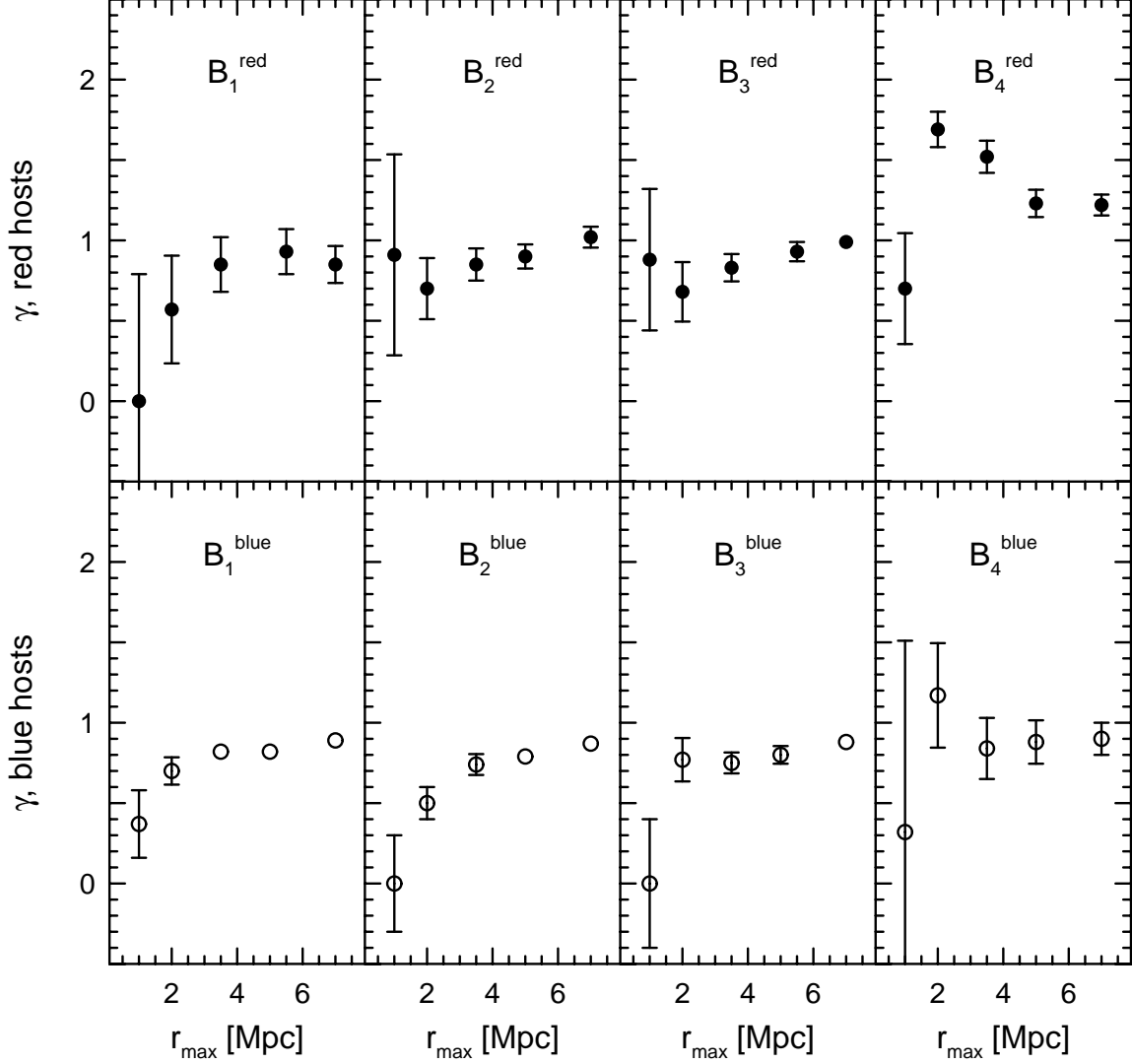


Fig. 9.— Best-fitting values of the power-law index, γ , as a function of r_{max} for satellites surrounding hosts of different stellar masses. Here a fit to the 3D satellite locations has been performed. Error bars are omitted when they are comparable to or smaller than the sizes of the data points. With the exception of the satellites of the B_4^{red} hosts, for $r_{\text{max}} \geq 3.5$ Mpc the best-fitting values of γ are only weakly-dependent upon the value of r_{max} .

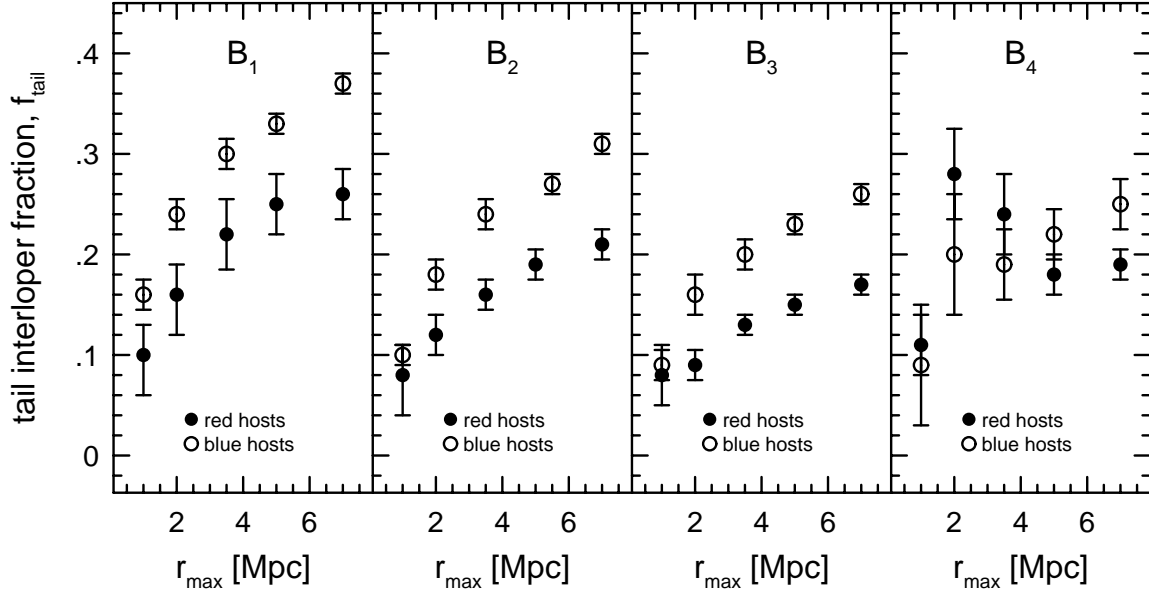


Fig. 10.— Best-fitting values of the tail interloper fraction, f_{tail} , as a function of r_{max} for satellites surrounding hosts of different stellar masses. Here a fit to the 3D satellite locations has been performed. With the exception of the satellites of the B_4^{red} host, the best-fitting values of f_{tail} increase monotonically with r_{max} , as expected.

a strong color-color correlation for hosts and their satellites (i.e., the satellites of red hosts tend to be red, while the satellites of blue hosts tend to be blue; e.g., Weinmann et al. 2006) and the interloper contamination is known to be considerably larger amongst blue satellites than it is amongst red satellites (e.g., AB10).

We quantify the quality of the model fits that are shown in Figures 8, 9, and 10 by computing the KS statistic, combined with 2,500 bootstrap resamplings. From this, all of the best-fitting models in Figures 8, 9, and 10 have KS rejection confidence levels of $(1 - P_{\text{KS}}) \times 100\% < 76\%$ (i.e., in all cases the fits are satisfactory). In particular, the quality of the fit is unaffected by our choice of the value for r_{max} . We also note that acceptable fits to the 3D satellite distribution require the presence of both the NFW and the tail interloper components. That is, acceptable model fits to the 3D distribution of the satellites cannot be obtained if we simply set $f_{\text{tail}} = 0$ (i.e., an “NFW-only” model) or $f_{\text{tail}} = 1$ (i.e., a “power-law only” model).

From Figure 8, the 3D fits to the satellite distributions yield best-fitting values of r_s that are insensitive to our choice of r_{max} . From Figure 9, the best-fitting values of γ are nearly identical for $r_{\text{max}} \geq 3.5$ Mpc (again with the exception of the satellites around the B_4^{red} hosts). Therefore, in Table 3 we show as examples the values of the KS rejection confidence levels for the 3D model fits, specifically using $r_{\text{max}} = 3.5$ Mpc. The columns of Table 3 indicate the host stellar mass bin, the confidence level at which the model can be rejected when γ is allowed to vary, and the confidence level at which the model can be rejected when γ is fixed at a value of 0.8 (i.e., consistent with the best-fitting value of γ for all but the satellites of the B_4^{red} hosts when we adopt $r_{\text{max}} = 3.5$ Mpc; see Figure 9). From Table 3, then, with the exception of the satellites of the B_4^{red} hosts with $\gamma = 0.8$, the KS rejection confidence level is $(1 - P_{\text{KS}}) \times 100\% < 72\%$, indicating good fits. In the case of the satellites of the B_4^{red} hosts, the best-fitting value of the power law index is actually $\gamma = 1.5 \pm 0.1$ for $r_{\text{max}} = 3.5$ Mpc. Hence, when we fix γ to be 0.8 for the satellites of the B_4^{red} hosts, the model is rejected at a modest confidence level (95%; see Table 3).

Figure 11 shows the dependence of the best-fitting values of r_s and f_{tail} on host stellar mass. From the top panel of Figure 11, the dependence of the NFW scale radius on host stellar mass is well-fitted by a power law, but the index of the power law differs for the red and blue hosts. Formally, we have $\log_{10} r_s^{\text{red}} = (0.71 \pm 0.05) \log_{10} [M_*/M_\odot] - (6.0 \pm 0.6)$ for the satellites of the red hosts and $\log_{10} r_s^{\text{blue}} = (0.48 \pm 0.07) \log_{10} [M_*/M_\odot] - (3.8 \pm 0.8)$ for the satellites of the blue hosts. From Figure 11, it is also clear that for host stellar masses $M_* \gtrsim 4 \times 10^{10} M_\odot$, the satellite distribution around blue hosts is much more concentrated than is the satellite distribution around red hosts, where the concentration is defined in the standard way: $c = r_{200}/r_s$ (see Tables 1 and 2 for the mean values of r_{200} in each of the

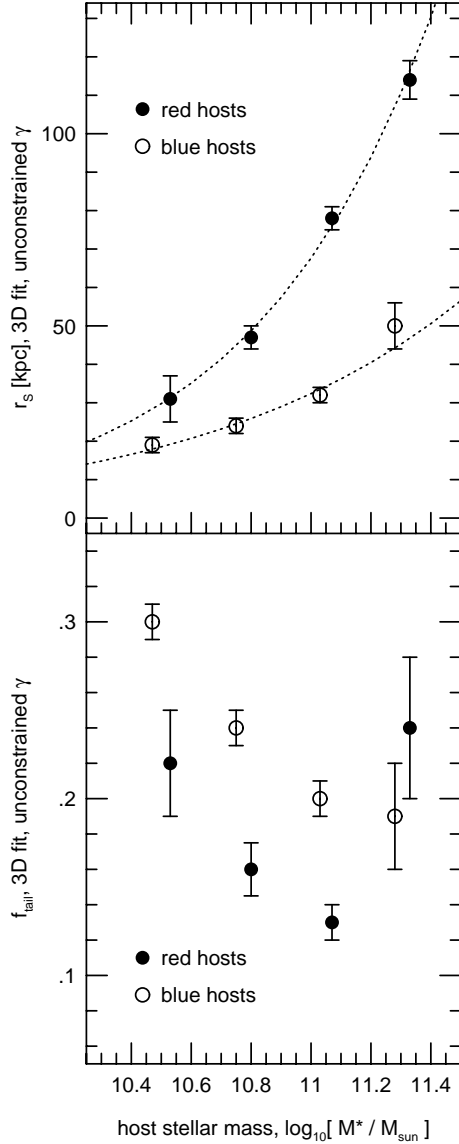


Fig. 11.— Best-fitting values of the model parameters r_s and f_{tail} as a function of host stellar mass, obtained for $r_{\text{max}} = 3.5$ Mpc. Here fits to the satellite locations in 3D have been performed and the model parameter γ has been allowed to vary. Different point types correspond to hosts of different colors (solid circles: red hosts; open circles: blue hosts). *Top*: NFW scale parameter, r_s . Dotted lines show the best-fitting power laws for the dependence of r_s on host stellar mass. *Bottom*: Tail interloper fraction, f_{tail} . The value of f_{tail} for the red hosts with the highest stellar masses falls far from the general trend of f_{tail} with host stellar mass. This is likely due to the sample of satellites for these particular hosts being incomplete (see text).

stellar mass bins). From the bottom panel of Figure 11, with the exception of the satellites of the B_4^{red} hosts, the tail interloper fraction decreases monotonically with host stellar mass.

Figure 12 shows the values of r_s and f_{tail} that are obtained when we perform fits to the 3D locations of the satellites and allow the value of γ to vary, versus those that are obtained when we simply fix the value of γ to be 0.8 (i.e., reducing the number of parameters in the model by one). With the exception of the satellites of the B_4^{red} hosts, fixing γ to be 0.8 yields values of r_s and f_{tail} that agree well with the values obtained from the fits in which γ is allowed to vary. Being able to reduce the number of parameters in the model by fixing the value of γ will be useful when we perform model fits to the projected locations of the satellites (i.e., the 2D distribution) below. This is due to the fact that the projected data from an observational sample are unable to constrain all of the parameters of the model independently. That is, on large scales both f_{tail} and γ contribute significantly to the shape of the probability distribution for the projected satellite locations, $P_{2D}(R_p)$. However, the projected data cannot constrain the value of γ uniquely while simultaneously allowing the value of f_{tail} to vary (and vice versa).

In order to obtain best-fitting models for the 2D locations of the satellites, we define a probability density function of the form

$$P_{2D}(R_p) \equiv (1 - f_{\text{tail}}) \frac{2\pi R_p \Sigma_{\text{NFW}}(R_p)}{N_{\text{p,NFW}}(<R_{\text{max}}) - N_{\text{p,NFW}}(<R_{\text{min}})} + f_{\text{tail}} \frac{2\pi R_p \Sigma_{\text{tail}}(R_p)}{N_{\text{p,tail}}(<R_{\text{max}}) - N_{\text{p,tail}}(<R_{\text{min}})} . \quad (18)$$

As with the fits to the 3D satellite distributions above, we again implement a ML procedure to find the best-fitting model parameters. We fix γ to be 0.8 and we obtain fits for f_{tail} and r_s from the projected radial locations of the satellites (i.e., here we use all satellites along the line of sight since the physical distances between hosts and satellites are not included in the 2D data set). Recall that above the values of R_{min} and R_{max} for the satellites were chosen to be 25 kpc and 500 kpc, respectively. Taking $Z_{\text{max}} = r_{\text{max}} = 3.5$ Mpc in equations (13)-(16), then, we obtain good model fits and, again with the exception of the satellites of the B_4^{red} hosts, the best-fitting values of r_s from the projected satellite distributions are in good agreement with those obtained from the 3D distribution. KS rejection confidence levels for the fits to the 2D satellite distributions are shown in Table 4, and comparisons of the model parameters r_s and f_{tail} obtained from the 2D and 3D fits are shown in Figure 13.

From the top panel of Figure 13, we conclude that, except in the case of the satellites of the most massive red hosts (for which our sample is likely to be incomplete), fitting the projected (2D) satellite locations with a combination of an NFW component and a power-law component with $\gamma = 0.8$ recovers the values of the NFW scale radius that one would obtain if one knew the full 3D distribution of the satellites. In the case of the satellites of

Table 3. 3D Model Rejection Confidence Levels, $r_{\max} = 3.5$ Mpc

Bin	$(1 - P_{\text{KS}}) \times 100\%$ unconstrained γ	$(1 - P_{\text{KS}}) \times 100\%$ $\gamma = 0.8$
B_1^{red}	46%	45%
B_2^{red}	3%	4%
B_3^{red}	25%	27%
B_4^{red}	47%	95%
B_1^{blue}	68%	65%
B_2^{blue}	60%	72%
B_3^{blue}	30%	43%
B_4^{blue}	1%	2%

Table 4. 2D Model Rejection Confidence Levels, $Z_{\max} = 3.5$ Mpc, $\gamma = 0.8$

Bin	$(1 - P_{\text{KS}}) \times 100\%$
B_1^{red}	6%
B_2^{red}	22%
B_3^{red}	9%
B_4^{red}	28%
B_1^{blue}	27%
B_2^{blue}	5%
B_3^{blue}	1%
B_4^{blue}	1%

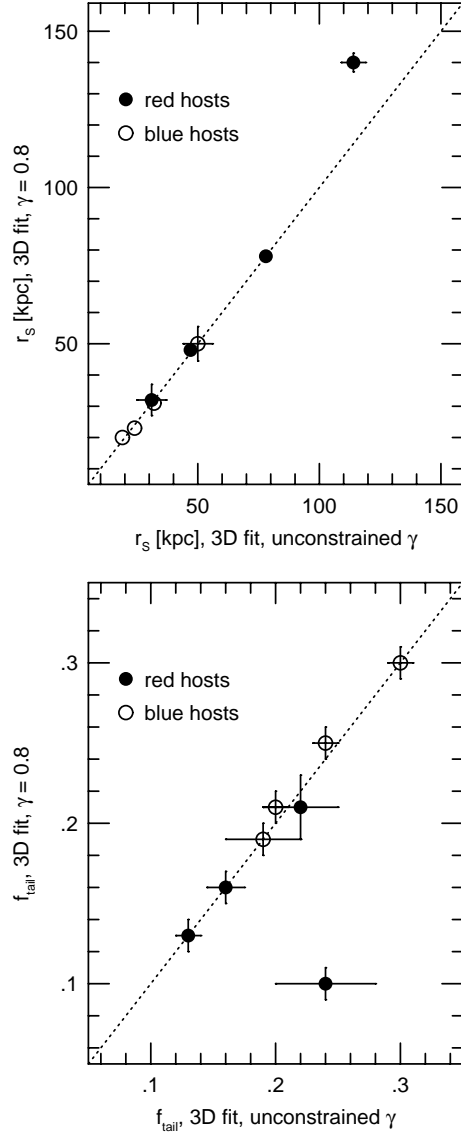


Fig. 12.— Comparison of best-fitting values of the model parameters r_s and f_{tail} obtained when the parameter γ is allowed to vary (abscissas) and when γ is fixed to a value of 0.8 (ordinates). Here fits to the satellite locations in 3D were performed and a value of $r_{\text{max}} = 3.5$ Mpc was adopted. Different point types correspond to hosts of different colors (solid circles: red hosts; open circles: blue hosts). Solid circles that lie far away from the general trend correspond to fits to the locations of the satellites of the most massive red hosts (stellar mass bin B_4^{red}) for which $\gamma = 0.8$ is a poor fit (see text and Table 3). *Top*: NFW scale parameter, r_s . *Bottom*: Tail interloper fraction, f_{tail} .

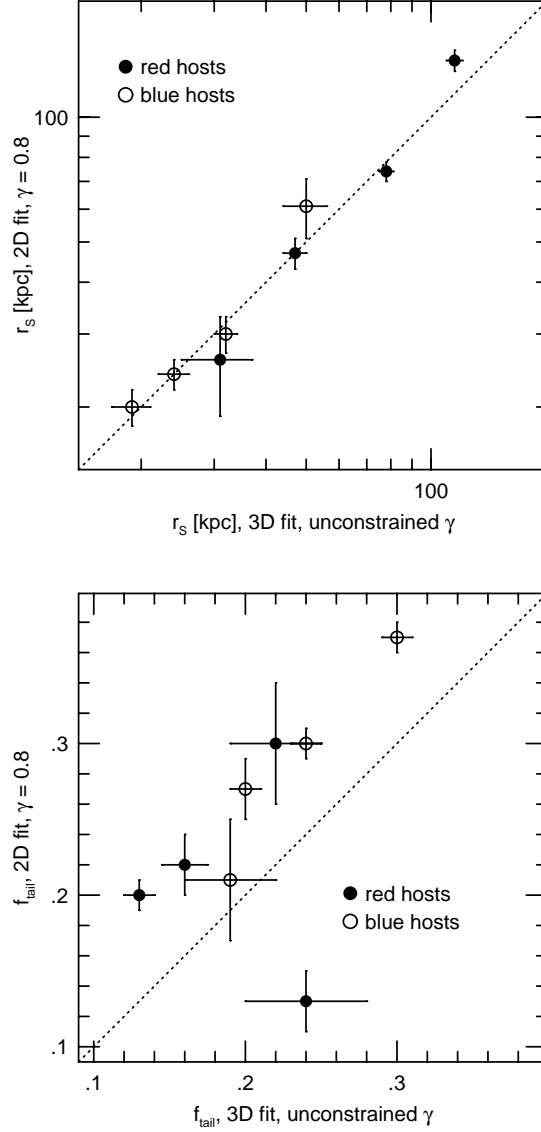


Fig. 13.— Comparison of best-fitting values of the model parameters r_s and f_{tail} obtained from fits to the 3D and 2D (i.e., projected) locations of the satellites. Here values of $r_{\text{max}} = Z_{\text{max}} = 3.5$ kpc have been adopted. In the 3D fits the value of γ is allowed to vary, but in the 2D fits the value of γ is fixed to 0.8 since γ and f_{tail} cannot be obtained independently of one another. Different point types correspond to hosts of different colors (solid circles: red hosts; open circles: blue hosts). Solid circles that lie away from the general trend correspond to fits to the locations of the satellites of the most massive red hosts, for which $\gamma = 0.8$ is a poor fit (see text and Table 3). *Top*: NFW scale parameter, r_s . With the exception of the satellites of the B_4^{red} hosts, the values of r_s obtained from the 2D and 3D fits agree to within $\sim 1\sigma$. *Bottom*: Tail interloper fraction, f_{tail} . With the exception of the satellites of the B_4^{red} hosts, the values of f_{tail} from the 2D fits exceed those from the 3D fits due to the fact that the 2D fits include all of the satellites, not just those with 3D distances $r \leq 3.5$ Mpc.

the B_4^{red} hosts, the two values of r_s disagree at the $\sim 2\sigma$ level ($r_s = 114 \pm 5$ kpc for the 3D fit and $r_s = 137 \pm 8$ kpc for the 2D fit). In other words, with the exception of the satellites of the B_4^{red} hosts, Figure 13 suggests that, provided the data sets are sufficiently large, one can accurately recover the values of r_s from observed host-satellite data sets when the satellites are selected using redshift space criteria (i.e., a satellite population that consists of both genuine satellites and correlated interlopers).

From the bottom panel of Figure 13, the values of f_{tail} that are obtained with the 2D fits to the satellite locations generally exceed those obtained with the 3D fits (the exception again being the satellites of the B_4^{red} hosts). This is due to the fact that in the 3D fits we used a 3D maximum distance of $r_{\text{max}} = 3.5$ Mpc and, hence, 6% of the total number of satellites (i.e., those with 3D distances $r > 3.5$ Mpc) were explicitly excluded from the 3D fits. In the case of the 2D fits, however, we must necessarily use all of the satellites along the line of sight since the fits are based solely upon the use of the projected locations of the satellites relative to their hosts. Therefore, we naturally expect f_{tail} to be larger for the 2D fits than for the 3D fits simply because of the presence of objects with $r > 3.5$ Mpc in the 2D data.

3.4. Dark Matter Distribution vs. Satellite Distribution

The results of §3.3 are “good news” in the sense that, even in the presence of a large number of interlopers (such as would be expected in a realistic observational sample), the scale radii of the satellite distributions obtained from 2D data alone accurately reproduce the scale radii that would be obtained if full 3D information for the satellite locations were known. Therefore, we would expect to be able to obtain accurate measurements of the scale radii of satellite samples that are selected from sufficiently large redshift surveys of the observed universe.

In addition to simply determining the spatial distribution of satellite galaxies that have been selected from redshift space, one might also hope to use the spatial distribution of the satellites to directly constrain the concentration of the dark matter halos that surround the host galaxies. This would, of course, be possible if the satellite galaxies faithfully traced the distribution of the dark matter. A number of studies of the locations of luminous satellite galaxies in semi-analytic models have led to the conclusion that, on the whole, when the satellites are selected using their 3D spatial locations, they trace the distribution of CDM halos quite well, both within galaxy clusters (e.g., Gao et al. 2004) and in lower density environments (e.g., Kang et al. 2005; Sales et al. 2007).

As discussed in §2, however, the satellites that we investigate here do not constitute a random subset of all luminous satellite galaxies. Rather, our satellites constitute only the brightest objects that would be selected using 3D spatial information and, hence, it is possible that the spatial distribution of these particular satellites may lead to different conclusions about the degree to which the satellite distribution traces the distribution of the underlying dark matter. For example, Sales et al. (2007) investigated the average satellite luminosity as a function of radius in their sample of 3D selected satellites. Averaged over their entire host-satellite sample, Sales et al. (2007) found clear evidence of luminosity segregation, with the average satellite luminosity dropping by a factor of order 2 between the host centers and their halo virial radii. Hence, their faintest and brightest satellites had different radial distributions on average.

Here we compute the scale radii for the dark matter halos of our host galaxies and we compare them to the scale radii of the satellite galaxy distributions that we obtained previously. To compute the scale radii of the halo dark matter distributions, we use the dark matter particles that AB10 found within the host halos to obtain best-fitting NFW mass profiles, averaged within each of the stellar mass bins. Figure 14 shows a comparison of the mean values of r_s obtained for the host halos using the dark matter particles (abscissa) and the mean values of r_s obtained for the satellite distributions (ordinate). Open circles show the results for blue hosts; filled circles show the results for red hosts. Here the scale radii of the satellite distributions are those that were computed using the 3D fits in §3.3 above. Since the scale radii of the satellite distributions increase monotonically with stellar mass (e.g., Figure 11), it is clear from Figure 14 that the scale radii of the halos also increase monotonically with stellar mass, as would be expected. From Figure 14, the distribution of satellites around the red hosts traces the dark matter distribution well. However, the scale radii for the dark matter distributions surrounding the blue hosts exceed those of the satellites by a factor of ~ 2 in all four stellar mass bins. This leads to the conclusion that, when selected in redshift space, the satellites of blue host galaxies have a spatial distribution that is approximately twice as concentrated as the dark matter that surrounds the blue hosts. Table 5 summarizes the mean values of the scale radii of the halo dark matter distributions ($r_{s,dm}$; column 2), the mean values of the scale radii of the satellite distributions ($r_{s,stat}$; column 3), and the corresponding mean values of the concentration parameters (c_{dm} and c_{sat} ; columns 4 and 5, respectively).

As mentioned in §2 above, our host galaxies are not selected to be “average” galaxies. Rather they are large, bright galaxies that are relatively isolated within their local regions of space. Because of this we would not necessarily expect the properties of their dark matter halos to be identical to the average population in the MRS. To explore this, we next compare the mean concentration parameters that we obtain for our host halos to the mean

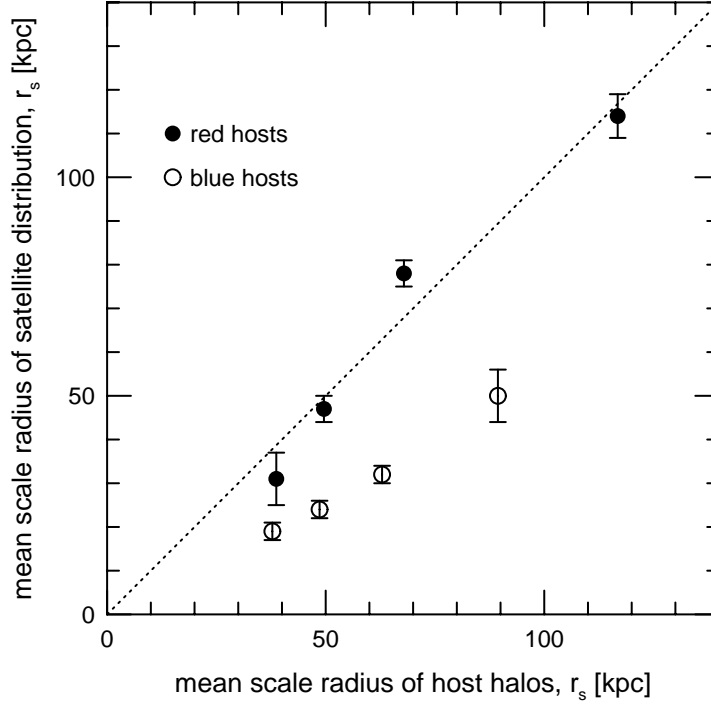


Fig. 14.— Comparison of scale radii for the satellite distributions and the dark matter halos that surround the hosts. Here r_s for the hosts has been calculated from the dark matter particles that are found within the halos. The satellites of red hosts are distributed similarly to the dark matter; however, the satellites of blue hosts have distributions that are more concentrated than the dark matter by a factor of ~ 2 .

Table 5. NFW Model Parameters for Satellites and Host Dark Matter Halos

Bin	$r_{s,dm}$	$r_{s,sat}$	C_{dm}	C_{sat}
B_1^{red}	38.7 ± 0.3	31 ± 6	5.83 ± 0.05	7.3 ± 1.4
B_2^{red}	49.6 ± 0.2	47 ± 3	5.74 ± 0.02	6.1 ± 0.4
B_3^{red}	67.9 ± 0.2	78 ± 3	5.42 ± 0.02	4.7 ± 0.2
B_4^{red}	116.8 ± 0.5	114 ± 5	4.71 ± 0.02	4.8 ± 0.2
B_1^{blue}	37.8 ± 0.1	19 ± 2	5.15 ± 0.01	10.3 ± 0.5
B_2^{blue}	48.6 ± 0.1	24 ± 2	4.91 ± 0.01	10.0 ± 0.8
B_3^{blue}	62.9 ± 0.2	32 ± 2	4.68 ± 0.01	9.2 ± 0.6
B_4^{blue}	89.4 ± 0.3	50 ± 6	4.59 ± 0.01	8.2 ± 1.0

concentration parameters obtained by Neto et al. (2007) for all MRS halos. Shown in both panels of Figure 15 are the mean values of the concentration parameters of our host halos as a function of M_{200} (solid circles: halos of red hosts; open circles: halos of blue hosts). Error bars are omitted for the mean values of the host halo concentration parameters because they are smaller than the sizes of the data points. Also shown in Figure 15 are the mean values of the concentration parameter and the corresponding 25th to 75th percentile range for the MRS halos obtained by Neto et al. (2007). Compared to the results for all MRS halos (open diamonds and dotted vertical lines in the top panel of Figure 15), the mean concentration parameters for the halos of our blue hosts fall far below the results for all MRS halos and the mean concentration parameters for the halos of our red hosts fall somewhat below the results for all MRS halos. The bottom panel of Figure 15 shows the Neto et al. (2007) halo concentration results separately for relaxed halos (plus signs and dotted vertical lines) and unrelaxed halos (triangles and dotted vertical lines). Within the halo mass range we study here, Neto et al. (2007) find that a fraction $f_{\text{unrelax}} \simeq 0.25$ of all MRS halos are unrelaxed.

From the bottom panel of Figure 15, the dependence of the mean host halo concentration parameter on M_{200} for the halos of blue hosts is consistent with the results for unrelaxed MRS halos. Therefore, it is likely that our sample of blue host galaxies is dominated by objects with unrelaxed halos, in which case we would not necessarily expect the spatial distribution of the satellites to trace the distribution of the dark matter. For the red host galaxies, the dependence of the mean halo concentration parameter on M_{200} is consistent with the upper (75%) bound on the value of c for unrelaxed MRS halos, but slightly below the lower (25%) bound on the value of c for all MRS halos. This suggests that the halos of our red hosts consist of a mixture of relaxed and unrelaxed halos, with a larger fraction of the halos of red hosts being unrelaxed in comparison to the complete sample of MRS halos (i.e., $f_{\text{unrelax}} > 0.25$ for the halos of our red host galaxies).

In their study of 3D selected satellites from the MRS, Sales et al. (2007) concluded that, when averaged over their entire host-satellite sample, the satellite distribution was slightly less concentrated than the average host dark matter halo ($c_{\text{sat}} \sim 5.6$ vs. $c_{\text{dm}} \sim 8.1$). They also found that dividing their host sample in half by either halo mass or host galaxy luminosity resulted in little change in the inferred concentration for the satellite distribution. Sales et al. (2007) did not investigate the concentration of the satellite distribution as a function of host stellar mass or color, so a direct comparison of our results and theirs is limited. From Table 5, the concentration of our satellite distributions appears to decrease somewhat with host halo mass (i.e., although the bins are based on the stellar masses of the hosts, the mean host halo mass increases by a factor of ~ 12.5 from bin B_1^{red} to bin B_4^{red} and by a factor of ~ 8 from bin B_1^{blue} to bin B_4^{blue} ; see Tables 1 and 2), however the effect is marginal (less than 2σ). Therefore, like Sales et al. (2007), we find no strong evidence that the concentration

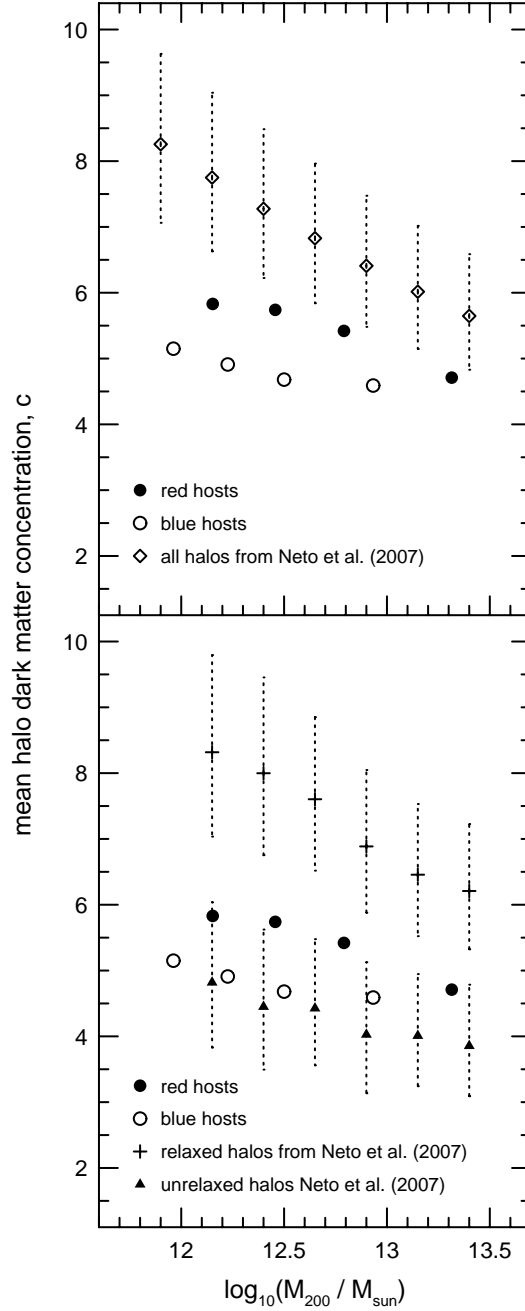


Fig. 15.— Comparison of mean host halo concentration parameters with the concentration parameters obtained for all MRS halos by Neto et al. (2007). Open circles: halos of blue host galaxies. Filled circles: halos of red host galaxies. Error bars for the mean host halo concentration parameters are omitted because they are smaller than the sizes of the data points. Dashed vertical lines indicate the range of values for c that correspond to the 25th and 75th percentiles from Neto et al. (2007). *Top*: Mean host halo concentration parameters compared to the concentration parameters of all halos from Neto et al. (2007; open diamonds). *Bottom*: Mean host halo concentration parameters compared to the concentration parameters of relaxed halos (plus signs) and unrelaxed halos (triangles) from Neto et al. (2007).

of the satellite distribution varies as a function of host halo mass. When we compute the mean value of the concentration parameter for our entire satellite distribution (weighted according to the number of satellites within r_{200} in each stellar mass bin), the result is similar to the mean value of the concentration for our entire host dark matter halo sample (weighted by the number of hosts within each stellar mass bin): $c_{sat} = 6.3$ vs. $c_{dm} = 5.2$. That is, when averaged over the entire sample, the distribution of our satellites is slightly more concentrated than is the dark matter that surrounds the host galaxies; however, the halos of our host galaxies are somewhat less concentrated than are the halos studied by Sales et al. (2007). Therefore, to the degree that our results and those of Sales et al. (2007) can be directly compared, we find broad general agreement.

4. Summary and Discussion

We have investigated the spatial locations of the satellites of relatively isolated “host” galaxies using a large sample of host and satellite galaxies selected from the first Millennium Run simulation (MRS). The satellites were identified using redshift space selection criteria, in direct analogy with spectroscopically selected satellite galaxies that have been identified in large redshift surveys. Selecting the satellites via redshift space criteria (rather than 3D distances) results in a geometry for the locations of the satellites that is essentially spherical for small physical separations and is cylindrical for large physical separations. The distinct change in geometry that occurs for the satellite locations at large distances from their hosts is accounted for explicitly in our model for the satellite locations. Our primary conclusions center on the answers to three questions: [1] How does the spatial distribution of the satellite galaxies depend upon the color and stellar mass of the host galaxy? [2] Can the parameters associated with the spatial distribution of the satellite galaxies obtained with full 3D information be accurately recovered when only projected (i.e., 2D information) is used? and [3] To what degree does the satellite distribution trace the distribution of the dark matter surrounding the halos of the host galaxies? We summarize the answers to these questions below.

As expected from previous work, we find that the 3D locations of the satellites are well-fitted by a combination of an NFW profile and a power law. The NFW profile characterizes the genuine satellites, while the power law characterizes the interlopers (or “false” satellites). The two-component model that we have adopted is a simplification of a triple power law of the form

$$\nu(r) \equiv A \frac{1 + (r/r_t)^{3-\gamma}}{r/r_s(1 + r/r_s)^2} = \frac{A}{r/r_s(1 + r/r_s)^2} + A \left(\frac{r_s}{r_t}\right)^3 \frac{r^2}{(r + r_s)^2} \frac{r_t^\gamma}{r^\gamma} \quad (19)$$

where r_t is a “tail radius” that characterizes the transition from the NFW regime of the satellite number density distribution to the tail interloper regime (see Ágústsson 2011). Although all of the analysis we have presented here can be reproduced through the use of a triple power law, the expressions for the projected satellite number density that are obtained when using a triple power law are not analytic, unlike the expressions above.

When using the 3D locations of the satellite galaxies, we find that the best-fitting values of the NFW scale radius, r_s , are insensitive to the maximum distance, r_{\max} , that we adopt in our Maximum Likelihood analysis. With the exception of the satellites of the most massive red hosts (for which the satellite sample is likely incomplete), the best-fitting power law index, γ , is also largely insensitive to the value of r_{\max} that is adopted, provided $r_{\max} \geq 3.5$ Mpc (i.e., we need a sufficient number of interlopers to be present in the tail of the distribution in order for the fit to converge to a single value of γ). From the 3D locations of the satellites, the best-fitting values of the NFW scale radius are functions of both the stellar masses and the rest-frame colors of the host galaxies. At fixed host stellar mass, the values of r_s for the satellites of red hosts exceed those for the satellites of blue hosts. The dependence of r_s on host stellar mass is well-fitted by a power law, but the index of the power law differs for the satellites of the red and blue hosts: $r_s^{\text{red}} \propto (M_*/M_\odot)^{0.71 \pm 0.05}$ and $r_s^{\text{blue}} \propto (M_*/M_\odot)^{0.48 \pm 0.07}$. These relationships constitute semi-analytic predictions for the dependence of the spatial distribution of satellite galaxies that should be observed in our universe, if the satellite galaxies have been selected from redshift space and if the mass of our universe is dominated by CDM. In particular, we expect that in our universe the spatial distribution of the satellites of blue host galaxies with $M_* \gtrsim 4 \times 10^{10} M_\odot$ will be significantly more concentrated than the spatial distribution of the satellites of red host galaxies with similar stellar masses.

When using the 2D locations of the satellite galaxies (i.e., their projected locations relative to their hosts), we find that, again with the exception of the satellites of the most massive red hosts, we can accurately recover the best-fitting values of the NFW scale radius that we obtained when using the full 3D data. If the mass of the universe is dominated by CDM, then, we expect that within a sample of satellite galaxies that has been selected from redshift space, the satellite distribution will be well-fitted by a combination of an NFW profile and a power law. An analysis of a sample of spectroscopically-selected satellite galaxies from a sufficiently large redshift survey will then lead to best-fitting values of r_s that agree well with the values one would obtain if full 3D information for the locations of the observed satellites were available.

When we compare the scale radii of the satellite distributions to the scale radii of the dark matter halos that surround the host galaxies, we find that the satellites of red host

galaxies trace the dark matter distribution well. However, in the case of the satellites of blue host galaxies, the spatial distribution of the satellites is more concentrated than is the halo dark matter by a factor of ~ 2 . This suggests that, when selected using redshift space criteria, the spatial distribution of satellite galaxies may be a biased tracer of the dark matter distribution that surrounds blue host galaxies. From the dependence of the host halo concentration on virial mass, it is likely that our sample of blue host galaxies is dominated by objects with unrelaxed halos. Therefore, we would not necessarily expect the spatial distribution of the satellites of blue host galaxies to trace the distribution of the halo dark matter.

Ágústsson (2011) attempted to obtain values of r_s for the spectroscopically selected satellites of red and blue host galaxies in the 7th data release of the SDSS. However, due to the small size of the sample (1,201 red hosts with 1,875 satellites and 657 blue hosts with 877 satellites) and the fact that relatively few SDSS satellites could be identified at projected radii $25 \text{ kpc} \lesssim R_p \lesssim 75 \text{ kpc}$ (i.e., because of fiber collisions at small host-satellite separations), Ágústsson (2011) was unable to place strong constraints on the values of r_s for the SDSS satellite sample. A definitive measurement of any difference in the value of r_s for the spectroscopically selected satellites of red and blue host galaxies in our universe will require much larger samples than those used by Ágústsson (2011), including samples for which the satellite distribution at small projected radii is considerably more complete than it is in the SDSS.

Acknowledgments

We gratefully acknowledge partial support of this work by the National Science Foundation under NSF grant AST-0708468. We are also grateful for the hospitality and financial support of the Max Planck Institute for Astrophysics that allowed IA to work directly with the MRS particle files. The Millennium Simulation databases used in this paper, and the web application providing online access to them, were constructed as part of the activities of the German Astrophysical Virtual Observatory (GAVO).

REFERENCES

- Ágústsson, I. 2011, PhD thesis, Boston University
- Ágústsson, I. & Brainerd, T. G., 2006, ApJ, 644, L25
- Ágústsson, I. & Brainerd T. G., 2006, ApJ, 650, 550
- Ágústsson, I. & Brainerd T. G., 2010, ApJ, 709, 1321 (AB10)
- Ágústsson, I. & Brainerd, T. G., 2011, ISRN Astronomy & Astrophysics, vol. 2011, id # 958973 (doi: 10.5402/2011/958973)
- Azzaro, M., Patiri, S. G., Prada, F., & Zentner, A. R. 2007, MNRAS, 376, L43
- Babu, G. J. & Feigelson, E. D. 2006, in ASP Conf. Series. vol. 351, *Astronomical Data Analysis Software and Systems XV*, eds. C. Gabriel, C. Arviset, D. Ponz & S. Enrique, 127
- Bartelmann, M. 1996, AA, 313, 697
- Bett, P., Eke, V., Frenk, C. S., Jenkins, A., Helly, J. & Navarro, J. 2007 MNRAS, 376, 215
- Blaizot, J., Wadadekar, Y., Guiderdoni, B., Colombi, S. T., Bertin, E., Bouchet, F. R., Devriendt, J. E. G., & Hatton, S. 2005, MNRAS, 360, 159
- Budzynski, J. M., Koposov, S. E., McCarthy, I. G., McGee, S. L. & Belokurov, V. 2012, MNRAS, 423, 104
- Brainerd, T. G. & Specian, M. A. 2003, ApJ, 593, L7
- Brainerd, T. G. 2005, 628, L101
- Conroy, C. et al. 2005, ApJ, 635, 982
- Conroy, C. et al. 2007, ApJ, 654, 153
- Conroy, C., Gunn, J. E. & White, M. 2009, ApJ, 699, 486
- De Lucia, G., Springel, V., White, S. D. M., Croton, D., & Kauffmann, G. 2006, MNRAS, 366, 499
- Fukugita, M., Ichikawa, T., Gunn, J. E., Doi, M., Shimasaku, K. & Schneider, D. P. 1996, AJ, 111, 1748

- Gao, L., DeLucia, G., White, S. D. M. & Jenkins, A. 2004, MNRAS, 352, L1
- Guo, Q., White, S., Li, C. & Boylan-Kolchin, M. 2010, MNRAS, 404, 1111
- Guo, Q., Cole, S., Eke, V. & Frenk, C. 2011, MNRAS, 417, 370
- Hayashi, E. & White, S. D. M. 2008, MNRAS, 388, 2
- Hogg, D. W., Finkbeiner, D. P., Schlegel, D. J. & Gunn, J. E. 2001, AJ, 122, 2129
- Kang, X., Mao, S., Gao, L. & Jing, Y. P. 2005, AA, 437, 383
- Klypin, A. & Prada, F. 2009, ApJ, 690, 1488
- Lares, M., Lambas, D. G. & Domínguez, M. J. 2011, ApJ, 142:13
- Li, C., Kauffmann, G., Wang, L., White, S. D. M., Heckman, T. M. & Jing, Y. P. 2006, MNRAS, 373, 457
- Lilliefors, H. W. 1969, JASA, 64, 387
- McKay, T. A. et al. 2002, ApJ, 571, L85
- More, S., van den Bosch, F. C., Cacciato, M., Mo, H. J., Yang, X. & Li, R. 2009, MNRAS, 392, 801
- More, S., van den Bosch, F. C., Cacciato, M., Skibba, R., Mo, H. J. & Yang, X. 2011, MNRAS, 410, 210
- Nagai, D. & Kravtsov, A. V. 2005, ApJ, 618, 557
- Navarro, J. F., Frenk, C. S., White, S. D. M., 1995, MNRAS, 275, 720
- Navarro, J. F., Frenk, C. S., White, S. D. M., 1996, ApJ, 462, 563
- Navarro, J. F., Frenk, C. S., White, S. D. M., 1997, ApJ, 490, 493
- Neto, A. F., Gao, L., Bett, P., Cole, S., Navarro, J. F., Frenk, C. S., White, S. D. M., Springel, V. & Jenkins, A. 2007, MNRAS, 381, 1450
- Nierenberg, A. M., Aguer, M. W., Treu, T., Marshall, P. J. & Fassnacht C. D. 2011, ApJ, 731:44
- Nierenberg, A. M., Auger, M. W., Treu, T., Marshall, P. J., Fassnacht, C. D. & Busha, M. T. 2015, ApJ, 752:99

- Norberg, P., Frenk, C. S. & Cole, S. 2008, MNRAS, 383, 646
- Prada, F., Vitvitska, M., Klypin, A., Holtzman, J. A., Schlegel, D. J., Grebel, E. K., Rix, H.-W., Brinkmann, J., McKay, T. A. & Csabai, I. 2003, ApJ, 598, 260
- Sales, L. & Lambas, D. G. 2004, MNRAS, 348, 1236
- Sales, L. & Lambas, D. G. 2009, MNRAS, 395, 1184
- Sales, L., Navarro, J. F., Lambas, D. G., White, S. D. M. & Croton, D. J. 2007, MNRAS, 382, 1901
- Siverd, R., Ryden, B. & Gaudi, B. S. 2009, preprint, submitted to ApJ (arXiv:0903.2264)
- Skibba, R. A., van den Bosch, F., Yang, X., More, S., Mo, H. & Fontanot, F. 2011, MNRAS, 410, 417
- Smith, J. A. et al. 2002, AJ, 123, 2121
- Springel, V., et al. 2005, Nature, 435, 629
- Strateva I., et al., 2001, ApJ, 122, 1861
- Strauss, M. A., Weinberg, D. H. et al. 2002, AJ, 124, 1810
- Tal, T., Wake, D. A. & van Dokkum, P. G. 2012, ApJ, 751:L5
- van den Bosch, F. C., Norberg, P., Mo, H. J. & Yang, X. 2004, MNRAS, 352, 1302
- Wang, W., Jing, Y. P., Li, C., Okumura, T. & Han, J. 2011, ApJ, 734:88
- Wang, W. & White, S. D. M. 2012, MNRAS, 424, 2574
- Wang, W., Sales, L. V., Henriques, B. & White, S. D. M. 2014, MNRAS, 442, 1363
- Weinmann, S. M., van den Bosch, F. C., Yang, X., & Mo, H. J., 2006, MNRAS, 366, 2
- York, D. G. et al. 2000, AJ, 120, 1579